Journal of Colloid and Interface Science 594 (2021) 228–244

Contents lists available at ScienceDirect

Journal of Colloid and Interface Science

journal homepage: www.elsevier.com/locate/jcis

Regular Article

Capacitance enhancement of nitrogen-doped graphene oxide/magnetite with polyaniline or carbon dots under external magnetic field: Supported by theoretical estimation

Misganu Chewaka Fite[a], Toyoko Imae[a,b,c,*]

[a] Graduate Institute of Applied Science and Technology, National Taiwan University of Science and Technology, Taipei 10607, Taiwan
[b] Department of Chemical Engineering, National Taiwan University of Science and Technology, Taipei 10607, Taiwan
[c] Department of Materials Science and Engineering, National Taiwan University of Science and Technology, Taipei 10607, Taiwan

GRAPHICAL ABSTRACT

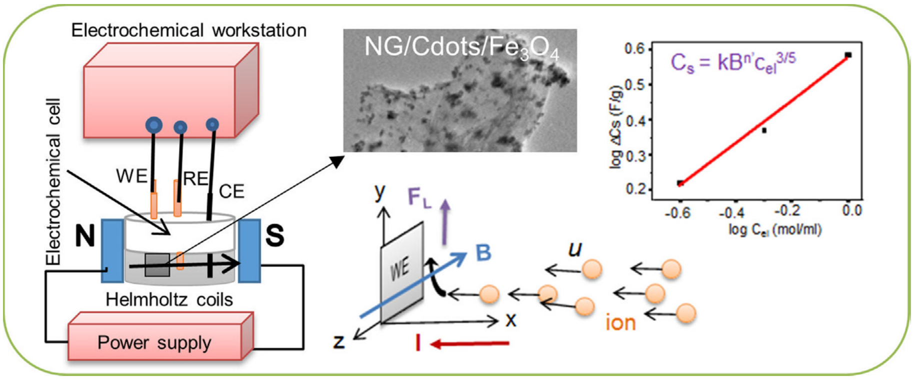

ARTICLE INFO

Article history:
Received 12 December 2020
Revised 12 February 2021
Accepted 24 February 2021
Available online 9 March 2021

Keywords:
Nitrogen-doped graphene oxide
Carbon dot
Polyaniline
Magnetite
Supercapacitor
Magnetic field

ABSTRACT

The effect of conductive materials (polyaniline (PA) or carbon dots (Cdots)) added to supercapacitor consisting of nitrogen-doped graphene oxide (NG) and magnetic nanoparticles (magnetite, Fe_3O_4) was assessed. Small amounts (4 wt%) of Cdots in composites of NG and Fe_3O_4 nanoparticles have shown better supercapacitor performance than the addition of PA. When the external stimulating force (magnetic field, 8.98 mT) was coupled with the electrochemical system, the specific capacitance was highest (2213 F/g at a scan rate of 5 mV/s) and the cyclic retention was 91% after 5000 cycles for the NG/Cdots/Fe_3O_4 composite electrode. These reports show that the adequate ternary composite materials effectively enhance the specific capacitance, increase the specific energy density and maintain the durability of supercapacitors under the magnet. The increase in the specific capacitance under the uniform magnetic field was proportional to the 3/5 power of bulk electrolyte concentration, although the power value was different from the theoretical estimation. The complex capacitance was almost double under the magnetic field due to the convection induced by the Lorentz force. It was also confirmed in comparison with the theoretical estimation that the Lorentz effect was responsible for the reduction of the charge transfer resistance, the increase of the relaxation time constant, the facilitation of the ion diffusion, and hence the increase of the double-layer capacitance. The present results will open a new window for the enhancement mechanisms on the capacitance efficiency under the magnetic field.

---

* Correspondence author at: Graduate Institute of Applied Science and Technology, National Taiwan University of Science and Technology, Taipei 10607, Taiwan.
E-mail address: imae@mail.ntust.edu.tw (T. Imae).

https://doi.org/10.1016/j.jcis.2021.02.112
0021-9797/

Nomenclatures

λ	x-Ray wavelength
Cs	Specific capacitance
Csg	Specific gravimetric capacitance
E	Specific energy density
P	Specific power density
I	Current
V	Potential
m'	Mass of electroactive material
ΔV	Potential window
v	Scan rate
i	Current density
t_{dc}	Discharge time
M	Magnetization
H	Magnetic field
d	Interlayer spacing
θ	Angle of d-spacing
R_s	Solution resistance
W_s	Warburg impedance
R_{ct}	Charge transfer resistance
Z'	Real impedance
Z''	Imaginary impedance
C'	Real capacitance
C''	Imaginary capacitance
a	Double-layer capacitance ratio constant
Q	Real capacitance ratio constant
S	Imaginary capacitance ratio constant
F	Frequency
B	External magnetic field
F_L	Lorentz force density
C_{el}	Electrolyte concentration
I_B	Current under external magnetic field
I_o	Current under normal condition
ΔI_B	Generated current under external magnetic field
$C_{S,B}$	Specific capacitance under external magnetic field
C_0	Specific capacitance in absence of external magnetic field
ΔC_B	Increase in specific capacitance due to external magnetic field and electrolyte
k, k', k'', b	Constants
R	Gas constant
h, n'	Arbitrary powers
T	Temperature
n	Number of electrons
m	Kinetic equation at normal condition
m_0	Intrinsic kinetic constant
m_B	Kinetic equation under magnetic field
F	Faraday constant
α	Cathodic charge transfer coefficient
β	Anodic charge transfer coefficient
I'	Electric current equation under normal condition
I_B'	Electric current equation under magnetic field
A	Electrode area
$C_p\ (0,t)$	Surface concentration of species on electrode at position x = 0 and time t
X	Position
t	Time
R_{ctB}	Charge transfer resistance under magnetic field
$V(t)$	Sinusoidal voltage
$I(t)$	Sinusoidal current
$Z(\omega)$	Complex impedance
Z_0	Complex impedance under normal condition
Z_B	Complex impedance under external magnetic field
V_B	Voltage under magnetic field
Z'_0	Real impedance under normal condition
Z''_0	Imaginary impedance under normal condition
$\Delta Z'_B$	Change in real impedance under normal condition
$\Delta Z''_B$	Change in imaginary impedance under magnetic field
j	Complex number
C_{dl}	Double-layer capacitance
C_{dl0}	Double-layer capacitance under normal condition
C_{dlB}	Double-layer capacitance under external magnetic field
$\Delta C'_B$	Change in real capacitance under normal condition
$\Delta C''_B$	Change in imaginary capacitance under external magnetic field
C'_0	Real capacitance under normal condition
C''_0	Imaginary capacitance under normal condition
C'_B	Real capacitance under external magnetic field
C''_B	Imaginary capacitance under external magnetic field

1. Introduction

Based on the huge consumption due to technological advancement and growing demand for portable electronic devices, the energy storage devices are the considerable request for the next generation [1,2] that attracts the research community to concentrate on the development and search of new sustainable energy storage devices. Among renewable energy storage devices, electrochemical capacitors or supercapacitors with high power density [3], long cycle life [4], and fewer equivalent series resistance [5] have drawn attention to increase the performance. The energy storage mechanism of a supercapacitor is highly dependent on the process at the electrode-electrolyte interface and in general can be classified into two categories; electrical double layer capacitance (EDLC: based on charge separation at the interface) and pseudocapacitance (PC: based on faradaic reaction at the interface). Owing to their good conductivity, long cycle stability and high specific surface area [3], carbon-based EDLC materials are the preferable selection for supercapacitor, although their specific capacitances [6] and energy densities are still minimal [4,7]. On the other hand, conductive polymers and metallic oxides/hydroxides are PC materials with high specific capacitance [8] but the poor cycle stability [9], and the capacitance retention [10] hinders their practical application. Such flaws will be mitigated by producing hybrid electrodes of PC and EDLC materials [11–15], but the specific capacitance, energy density, and power density of obtained hybrid electrides are still fewer. Carbon quantum dots (Cdots), which are defined as a class of carbon-based fluorescent material containing different functional groups (hydroxyl, carboxyl, amine, and so on), have attracted attention because of its exceptional electro-optical properties [16], ultrafast electron transfer [17], small size [18], cheapness, facile preparation [19], and favorability for potential applications [13,18–20].

Numerous studies have focused on the development of innovative materials for supercapacitors, and the obtained results lead us to look for a new methodology with efficient performance to enforce the efficiency of the newly emerging materials. Researchers have turned their attention to assist by means of external fields (electric, magnetic, light, and so on) to lower the activation potential barrier, to reduce the resistance, and so on. The electrical conductivity of a material is a response of electric current and specifies the easiness of conductance in a material, because the conductance is a basic indicator of charge/ion flow. The external magnetic field is of exceptional character to stimulate an electrolyte, to intensify the electrical current response, to increase conductance, and to facilitate the access of electrolyte ion into the electrode/electrolyte interface. Thus, it should efficiently enhance the formation of an electric double-layer and the capacitance on supercapacitor because of the Lorentz force effect.

When an external force is applied to an electrical current-carrying conductor, the velocity of the electric charge passing through a conductor, that is, electric current should increase. Since the external magnetic force exerts on an accelerating electric charge in a direction orthogonal to the magnetic field, it can cause the movement of electrolyte charges/ions to the electrode surface and produce the convection of an electrolyte. In recent years, the influence of an external magnetic field on the supercapacitor electrode has attracted attention. Zeng, et al. [4] have reported that the magnetic field (1.34 mT) has induced an impedance effect on an electrochemically deposited MnO_2 electrode, enhanced an interface charge density and facilitated an electrolyte transportation. Ahmed and Imae [13] have noticed that iron oxide nanoparticles in exfoliated graphene-based magnetic composites have shown better capacitance performance under the external magnetic field (maximum 1191 G). Zhu, et al. [21] have found an interfacial relaxation process restricted by a magnetic field (720 G) on graphene and magnetic graphene nanocomposite electrodes. Bin, et al. [22] have developed that the diffusion coefficients of cations can increase under the external magnetic field. Wei, et al. [23] have found that a magnetite/polypyrrole nanocomposite capacitor has increased significantly the energy density under the exertion of a magnetic field. Wang, et al. [24] have reported that a micro-magnetic field has improved the EDLC, reduced the charge transfer resistance and enhanced the discharge performance. Pal, et al. [25] have found that an external field (0.125 T) has allowed the electrolyte ions to go to the surface of the inaccessible reduced graphene oxide/Fe_3O_4 hybrid electrode. All reports indicated that the Lorentz effect is responsible. However, theoretical reasons have never been reported for the effect of the external magnetic field.

In previous article [11], the capacitance performance of NiO, Co_3O_4, and Fe_3O_4 hybridized to nitrogen-doped graphene oxide (NG) has been measured under the external magnetic fields (0, 8.98 mT). Then an NG/Fe_3O_4 hybrid material has shown the highest capacitance performance, although the efficiency was still not enough high, the stability under the external field was fluctuated, and the role of the magnetic field on enhancement was not clarified. To enhance the capacitive performance and to compensate the fluctuating stability under the magnetic field, the third component like a PC material and an EDLC material, respectively, should be added as hybrid materials. Cdots as an EDLC material and polyaniline (PA) as a PC material [4,12–15,20] are effective for improving the stability and the capacity, respectively. The added Cdots has enhanced the capacitance performance of carbon nanohorn/PA composites [26] and the photovoltaic effect of metal oxide dye-sensitized solar cells [18,27]. Thus, it is suggested that these materials can be used to promote the performance of an NG/Fe_3O_4 electrode material.

In this work, NG/Cdots/Fe_3O_4 and NG/PA/Fe_3O_4 ternary composites will be produced to study the capacitance performance. The electrodes of ternary composites are expected to show the anticipative specific capacitance and the better cycling retention. It can be also envisaged that the electrochemical measurements coupled with the applied external magnetic field will achieve the further enhancement of the specific capacitance and the cycling stability, although we have never known the reported capacitance results on NG/PA/Fe_3O_4 and NG/Cdots/Fe_3O_4 electrodes under the magnetic field. The trigger contributing to the enhancement by the external magnetic field will be elucidated with the aid of the additional electrochemical measurement and the theoretical estimations derived from the Lorentz force. These analyses will offer an easy and efficient way to improve the capacitance performance of hybrid materials under the added external physical field.

2. Experimental section

2.1. Reagents

Graphite flake (C > 99%) was a product from Japan (Ito graphene Co, Ltd.). Ferrous chloride tetrahydrate was purchased from Alfa Aesar, England. Aniline (99.5%), ferric chloride hexahydrate (99%), hexadecyl trimethyl ammonium bromide (CTAB, 99%), ammonium persulfate (APS, 98%), citric acid (CA), ethylenediamine (EDA) and *N*-methyl pyrrolidone (NMP) were from Acros organics, UK. A glass coated by indium tin oxide (ITO) was obtained from AimCore Technology, Taiwan. Polyvinylidene fluoride (PVDF) was the product from Sigma Aldrich, USA. Other reagents are commercial grade. All of the experimental solutions were prepared with ultrapure water (resistivity of 18.2 MΩ cm, Yamato Millipore WT100, Japan).

2.2. Synthesis of materials

NG is the same sample that was previously synthesized [11]. Briefly, graphene oxide was prepared from graphite flakes using a modified Hammers method, mixed with urea, dispersed in water and hydrothermally reacted overnight at 180 °C in a Teflon-lined autoclave. The characterization of product was reported in a previous report [11]. The composite consisting of NG and PA was prepared by in situ chemical polymerization [12]. The mixture of NG (183.6 mg) and CTAB (124 mg) in an aqueous 1 M HCl solution (31.25 ml) and aniline (60 µl) was stirred 1 h in an ice bath. After the dropwise addition of an initiator (APS, 204 mg) in 1 M HCl (6.25 ml), the mixture was kept stirring for a day at less than 5 °C. The resultant precipitate was filtered, washed several times with water and ethanol, and dried overnight at 50 °C. The composites of NG content x at 0, 25, 50, 75, and 100 wt% were prepared and named as NGx/PA.

Magnetite was deposited on NG75/PA by a co-precipitation technique [11]. Ferrous chloride tetrahydrate and ferric chloride hexahydrate (a mole ratio of 1:2) were added to an aqueous dispersion of NG75/PA (2 mg/ml, 100 mg) and stirred for 1 h at room temperature (~25 °C). Then, an aqueous ammonium solution was added, and the mixture was stirred at 80 °C for additional 1 h. The product was collected by the magnet, washed with water and dried overnight in a vacuum oven at 50 °C. The composites were prepared at Fe_3O_4 content y of 20, 33, 42, 50, and 60 wt% against NG75/PA and named as NG75/PA/Fe_3O_4y.

Cdots were synthesized hydrothermally [16,18] by heating CA (1.0 g) and EDA (174, 300, and 520 µl) in water (60 ml) in an autoclave at 230 °C for 5 h. The calculated mole ratios of EDA/CA were 0.5:1, 1:1, and 1.5:1, respectively. The brown powder of Cdots was collected by evaporating solvent in a rotary evaporator and dried in a vacuum oven at 40 °C. Cdots (2, 4, and 6 wt%) at EDA:CA of 1:1 were mixed with an aqueous dispersion of NG and named as NG/Cdots(1:1,2), NG/Cdots(1:1,4), and NG/Cdots(1:1,6), respectively. Then Fe_3O_4 was deposited on NG/Cdots(1:1,4) to prepare NG/Cdots(1:1,4)/Fe_3O_4y (y = 33, 42, and 50 wt%) composites by the co-precipitation technique described above [11]. Separately, NG/Cdots(0.5:1,4)/$Fe_3O_4$42 and NG/Cdots(1.5:1,4)/$Fe_3O_4$42 composites were also prepared as well.

2.3. Instruments

A transmission electron microscope (TEM, JEOL JSM-2000FX II, Japan) and a high-resolution TEM (HRTEM, JEOL, JEM-2000FXII, Japan) were operated at 120 and 200 kV accelerating voltages, respectively. A fluorescence (super high-pressure mercury lamp, Model C-SHG1, 100 W) microscope was a product of Nikon (Eclipse TE 2000-U, Japan). Fourier transform infrared (FTIR) absorption spectra (Nicolet Thermo Scientific, 6700, USA) were measured for KBr pellet. X-ray diffraction (XRD, D2 PHASER X-ray diffractometer, Germany) patterns were obtained using a Cu target (λ = 0.154 nm) at a scan rate of 0.1° $min^{-1}_{.}$ The nitrogen adsorption/desorption isotherms were measured at 77 K on a BELSORP-max instrument, Japan. The samples were heated at 110 °C for 3 h in a vacuum before the adsorption measurments. A Brunauer-Emmett-Teller (BET) and a Barrette-Joyner-Halenda (BJH) techniques were used to calculate the surface area and the pore size distribution, respectively. A magnetic hysteresis loop was recorded on a magnetic instrument (SQUID000100, Quantum Design, USA) with a magnetic field ranging from −20 to 20 kOe. A theta probe ESCA (VG Scientific ESCALAB 250, UK) was used to record X-ray photoelectron spectra (XPS). A DC power supply (Laboratory DC power supply GW Instek GPR-3060D, ITM Instruments INC., Canada) was connected to a Helmholtz coil (PASCO EM-6723 Field Coils, KYS Tech. Co. Ltd., Taiwan) to generate an external magnetic field.

2.4. Electrochemical measurements

Working electrodes were prepared by mixing composites (90 wt%) with polyvinylidene fluoride in *N*-methyl pyrrolidone (10 wt%), sonicating (Branson 1210 Ultrasonic Cleaner, Yamato, Japan) for 2 h and stirring overnight at 45 °C until homogenized. The slurry (20 μl) was cast on a cleaned ITO substrate (1 cm × 1 cm) and dried [11,28]. Then the average mass loading of active materials on the ITO substrate was 0.14 ± 0.02 mg. An electrochemical workstation (ZAHNER messsysteme, model XPot, Germany) was used for electrochemical measurements using a three-electrode system in a 1 M NaCl electrolyte solution. A composite-cast ITO substrate, an Ag/AgCl (3 M KCl), and a Pt wire were used as a working electrode, a reference electrode, and a counter electrode, respectively. The cyclic voltammetry (CV) was swept at 5–100 mV/s scan rates over a potential window of 0.8 V. A galvanostatic charge-discharge (GCD) was measured at current density range of 1–6 A/g. An electrochemical impedance spectroscope (EIS) was operated at a frequency range from 100 mHz to 100 kHz by applying an alternating current (AC) with an amplitude of 10 mV. An external magnetic field of 8.98 mT was generated in an electrochemical cell kept between two poles (north-N and south-S) of an electromagnet (Helmholtz coil) as reported in our previous work [11] and shown in Fig. 1. A specific capacitance Cs [F/g] from CV curves was calculated from Eq. (1a) [11,12,29]. Whereas, a specific gravimetric capacitance Csg [F/g], a specific energy density E [Wh/kg] and a specific power density P [W/kg] in the three-electrode system were calculated from Eqs. (1b)–(1d) [23];

$$\mathrm{Cs} = \frac{\int IdV}{m'v}\Delta V \tag{1a}$$

$$\mathrm{Csg} = \mathrm{i}\frac{t_{dc}}{\Delta V} \tag{1b}$$

$$\mathrm{E} = \frac{\mathrm{Csg}}{7.2}\Delta V^2 \tag{1c}$$

$$\mathrm{P} = 3600\frac{E}{t_{dc}} \tag{1d}$$

where I [A] = a current, V [V] = a potential, m' [g] = a mass of electroactive material, ΔV [V] = the potential window, v [V/s] = a scan rate, i [A/g] = a current density and t_{dc} [s] = a discharge time.

3. Results and discussion

3.1. Characterization of materials

Magnetite was deposited in situ on an NG75/PA and NG/Cdots composites, and products (NG/PA/Fe_3O_4 and NG/Cdots/Fe_3O_4) were characterized. Fig. 2Aa and Ba show TEM images of NG75/PA/$Fe_3O_4$42, and NG/Cdots(1:1,4)/$Fe_3O_4$42 nanocomposites, respectively. Both TEM images revealed the existence of spherical particles with an average diameter of 10.2 and 9.4 nm in a sheetlike texture, respectively, as shown in Fig. 2Ab and Bb. These particles can be assigned to Fe_3O_4 because their sizes are consistent with the previous report [11]. The sheetlike texture of NG75/PA/$Fe_3O_4$42 was covered by dense wire-like structures, which resulted from the deposition of PA. Whereas, the sheetlike texture of NG/Cdots (1:1,4)/$Fe_3O_4$42 was similarly flat to that of NG [11]. In addition, Fig. 2C shows an HRTEM image of a sheet surface of a NG/Cdots (1:1,4) nanocomposite. The image revealed small domains of less than 5 nm with an average d-spacing of 0.23 and 0.36 nm (Fig. 2C1 and C2) corresponding to (100) and (002) facets, respectively, of a graphitic structure [30], indicating the existence of Cdots in an NG/Cdots(1:1,4) nanocomposite, although Cdots were not recognized in a image of Fig. 2Ba. A magnetization-magnetic field (M−H) curve (Fig. 2D) for the NG75/PA/$Fe_3O_4$42 nanocomposite proved the saturation magnetization of 4.8 emu/g at an external magnetic field ranging from −20 to 20 kOe. A very small coercivity, a negligible retentivity, and no hysteresis loop indicate a superparamagnetic nature of magnetite in the composite. These natures can facilitate the fast ionic diffusion rate, being advantageous in supercapacitor performance [31].

The powder XRD patterns of NG75/PA/$Fe_3O_4$42 and NG/Cdots (1:1,4)/$Fe_3O_4$42 were compared with those of component nanomaterials in Fig. 3. Although the NG75/PA displayed some diffraction peaks at 2θ = 9.18–27.3°, these peaks come from the crystal planes of PA in its emeraldine salt [32]. Broad diffraction peaks of NG at 2θ = 24.3° (002) and 43.1° (004) [11] should be overlapped on XRD patterns of PA. On the other hand, an XRD pattern of NG75/PA/$Fe_3O_4$42 displayed Bragg peaks at 2θ = 18.2° (111), 30.1° (220), 35.5° (311), 43.1° (400), 53.4° (422), 57.0° (333), 62.6° (440) and 74.6° (533). The pattern is completely different from that of NG75/PA but these peaks were perfectly the same as those of cubic Fe_3O_4 (shown in JPCPDF No. 82-1553), although a weak and broad peak around 2θ = 25.3° should originate from NG75/PA. Like NG75/PA/$Fe_3O_4$42, an XRD pattern of NG/Cdots(1:1,4)/$Fe_3O_4$42 showed Bragg peaks of cubic Fe_3O_4 at 2θ = 35.5° (311) and 43.1° (400). A broad peak at 2θ = 25.3° originates in a (200) facet of NG and Cdots.

The FT-IR absorption spectra of PA, NG75/PA/$Fe_3O_4$42, NG/Cdots (1:1,4)/$Fe_3O_4$42, and Cdots(1:1) were shown in Fig. 4. The characteristic features in an FT-IR absorption spectrum of PA were vibration bands assigned to N—H (3465–3450 cm^{-1}), quinoid ring C═C (1594 cm^{-1}), benzenoid ring C═C (1492 cm^{-1}), C—N (1236 cm^{-1}), and N═Q═N (Q = quinoid ring, 1110 cm^{-1}) stretching modes and an aromatic C—H (out-of-plane, 601 cm^{-1}) bending mode. Whereas, an IR absorption spectrum of Cdots displayed bands at 3848 cm^{-1} (O—H/N—H stretching), 1648 cm^{-1} (C═O/C═N stretching), 1558 cm^{-1} (N—H bending/C═C stretching), 1392 cm^{-1} (C—N stretching), and 626 cm^{-1} (NH_2 bending) [33], corresponding to the vibration modes of graphitic, carboxylic and amine groups [20]. However, an NG content in an NG75/PA/$Fe_3O_4$42 nanocomposite was 75 wt% against 25 wt% PA, an NG/Cdots(1:1,4)/

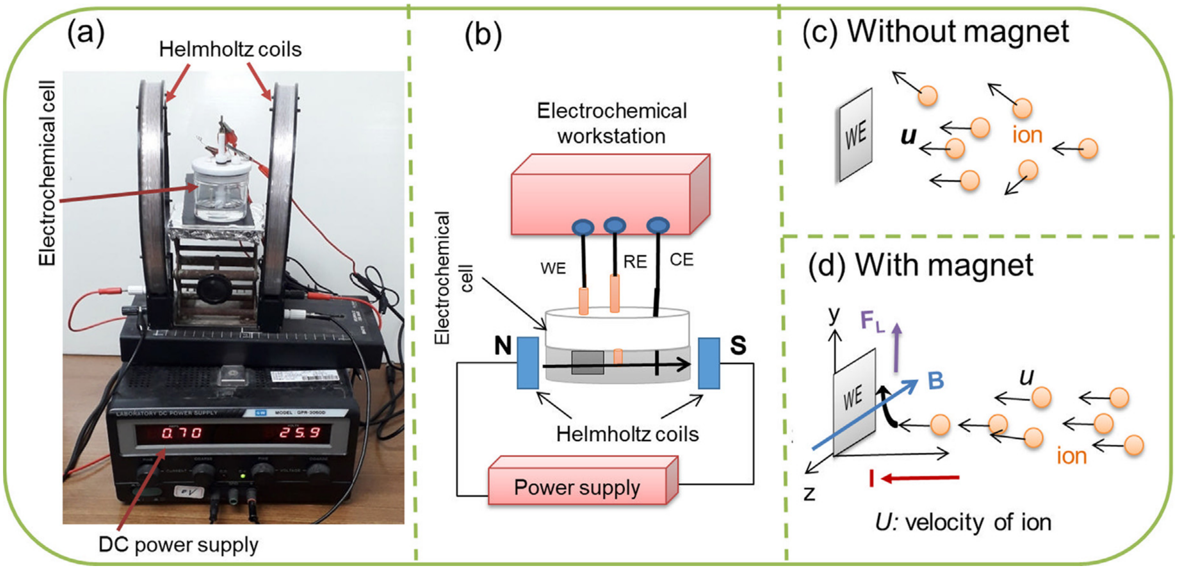

Fig. 1. (a) A photograph and (b) a scheme of an electrochemical cell setup equipped a magnetic field supply. The movement of ions at the conditions (c) without applying magnetic field and (d) with applying magnetic field. In Fig. 1c without a magnet field, ions move randomly and are governed by electrostatic force. Whereas, the movement of ions under the magnetic field (shown in Fig. 1d) is assisted by the Lorentz force (F_L), and the accessibility of ions to the electrode surface is accelerated. I: current, B: magnetic field.

$Fe_3O_4$42 nanocomposite consists of 96 wt% NG and 4 wt% Cdots, and both nanocomposites include 42 wt% Fe_3O_4 for NG75/PA or NG/Cdots(1:1,4). Thus, both IR spectra of NG75/PA/$Fe_3O_4$42 and NG/Cdots(1:1,4)/$Fe_3O_4$42 were mainly contributed by Fe_3O_4 and NG: They revealed IR bands at 3739 and 470–482 cm^{-1}, corresponding to an OH stretching mode of hydrated water on Fe_3O_4 and a Fe-O stretching mode [34], respectively, in addition of OH (3396 cm^{-1}) and C=C (1529 cm^{-1}) stretching modes of NG [11].

The chemical compositions and element states of NG75/PA/$Fe_3O_4$42 and NG/Cdots(1:1,4)/$Fe_3O_4$42 nanocomposites were analyzed by XPS, as shown in Fig. 5. A wide scan XPS spectrum of NG75/PA/$Fe_3O_4$42 (Fig. 5Aa) disclosed sharp peaks at 285, 399, 531, and 712 eV for C 1s, N 1s, O 1s, and Fe2p, respectively. Among deconvoluted peaks of Fe2p XPS spectrum (Fig. 5Ba), peaks at 711.2 and 725.5 eV are characteristics of Fe 2p3/2 and Fe 2p1/2 with satellite peaks at 719.1 and 733.2 eV, respectively, of magnetite nanoparticles [35,36]. Since the component of Fe_3O_4 is 42 wt% against NG75/PA (58 wt%), it is reasonable that the intensity of O 1s is highest. In fact, in the deconvoluted O1s spectrum, the main peak attributed to Fe-O was observed at 530.0 eV (Fig. 5Ca) but this peak was not observed in NG [11] and PA [37]. Other peaks at 530.6 and 532.2 eV can be assigned to C=O and O—H groups in NG. The results from O 1s and Fe 2p confirmed the existence of Fe_3O_4 in the composites. In addition, the second-strongest C 1s spectrum was deconvoluted into subpeaks of C=C/C—C aromatic (284.9 eV), C=N/C—N (285.3 eV), and C—O—C (286.7 eV) bonds of NG [11] and PA [37]. An N 1s spectrum of NG75/PA/$Fe_3O_4$42 was weaker than that of C 1s because of the fewer N contents in NG and PA, but the deconvoluted subpeaks at 398.4, 399.7 and 400.6 eV correspond to pyridinic, pyrrolic and amine bonds, respectively, of NG and PA. Especially, the occurrence of pyridinic binding energy at 398.4 eV proves the existence of PA, because pyridinic group exists only in a chemical structure of PA.

A wide scan XPS spectrum of NG/Cdots(1:1,4)/$Fe_3O_4$42 (Fig. 5Ab) was analogical to it of NG75/PA/$Fe_3O_4$42 due to the similarity of constituent bonds. However, the highest component, O 1s, was deconvoluted into four peaks, where three peaks at 530.0, 530.6 and 532.2 eV were attributed alike NG75/PA/$Fe_3O_4$42 but a peak at 534.0 eV could be assigned C—O—C of Cdots (Fig. 5Cb) [27]. In a deconvoluted N 1s spectrum of NG/Cdots(1:1,4)/$Fe_3O_4$42, peaks at 399.1, 400.8 and 402.6 eV were assigned to pyrrolic overlapped with C-NH_2, quaternary and oxidized-N bonds of NG [11] and Cdots [27]. An Fe 2p XPS spectrum and deconvoluted peaks (Fig. 5B) were completely the same between NG75/PA/$Fe_3O_4$42 and NG/Cdots(1:1,4)/$Fe_3O_4$42, indicating that the addition of PA or Cdots does not affect on the coexisting Fe_3O_4.

The detection of Cdots in an NG/Cdots/Fe_3O_4 composite is not necessarily confirmed perfectly from the characterization described above due to their small size (2–4 nm) and a similar composition against NG. Then the specific character of Cdots distinguishable from other components in composites is the strong fluorescence of Cdots [27]. Here the fluorescence microscopic images were observed for NG/Cdots(1:1,4), which was adsorbed on nonfluorescent cotton fibers [38]. As seen in Fig. 6, although similar fibers were observed on an optical microscopic observation of NG/Cdots(1:1,4)-adsorbed fibers, some of fibers displayed the significant luminescence on the fluorescence mode and they were distinguished from NG/Cdots(1:1,4)-unadsorbed fibers on the merged (optical + fluorescence) mode. The observed blue photoluminescence proves the existence of Cdots component. A similar examination was performed for Cdots(1:1)-adsorbed fibers and similar observations were obtained. Thus the results from microscopes, XRD, XPS, and IR absorption spectra described above demonstrate that the NG75/PA/$Fe_3O_4$42 and NG/Cdots(1:1,4)/$Fe_3O_4$42 composites were effectively synthesized through the in situ preparation methods.

3.2. Electrochemical characterization

The CV curves and specific capacitance of NGx/PA, NG75/PA/Fe_3O_4y, NG/Cdots(1:1,x), NG/Cdots(x:1,4)/$Fe_3O_4$42 and NG/Cdots(1:1,4)/Fe_3O_4y calculated using Eq. (1a) are shown in Fig. 7. All CV curves took quasi-rectangular shapes, indicating an EDLC feature due to the strong contribution of NG, and the specific capacitance always decreased with increasing scan rate due to the

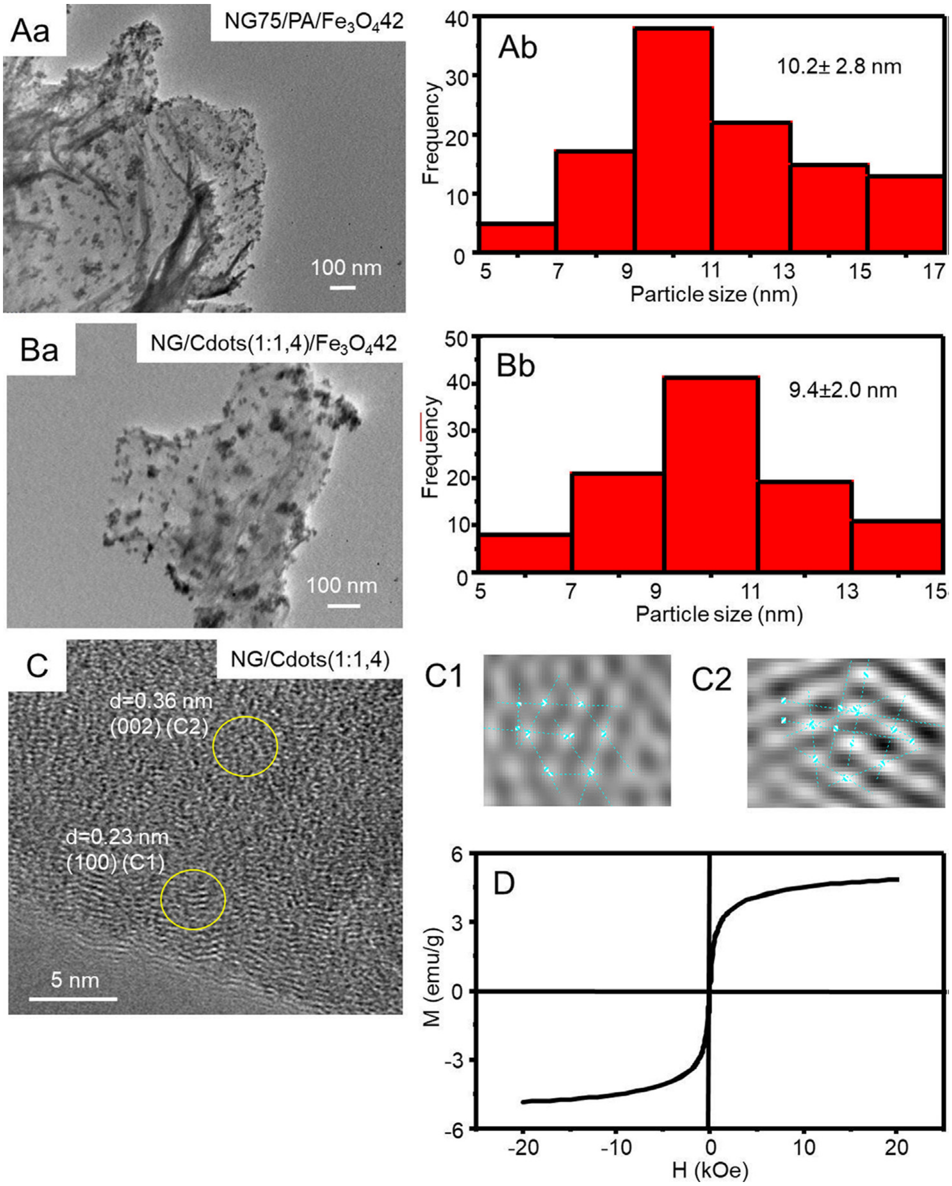

Fig. 2. (a) TEM images and (b) size-distribution histograms of Fe_3O_4 nanoparticles of (A) NG75/PA/$Fe_3O_4$42 and (B) NG/Cdots(1:1,4)/$Fe_3O_4$42. (C) An HRTEM of NG/Cdots (1:1,4). (C1) and (C2) Lattice parameters corresponding to (1 0 0) and (0 0 2) facets, respectively, of a graphitic structure. (D) A magnetization-magnetic field curve of NG75/PA/$Fe_3O_4$42.

insufficient time for transportation and the adsorption of electrolytes inside the electrodes [39], the relatively slower ion diffusion and the decreased utilization efficiency of the electrode material [40]. The specific capacitance calculated from the CV curve was superior at an NG:PA weight ratio of 75:25, and when Fe_3O_4 is added on NG75/PA, the highest specific capacitance was obtained at 42 wt% content of Fe_3O_4 for NG75/PA/Fe_3O_4. On the other hand, the specific capacitance of NG/Cdots electrode was highest at 4 wt% content of Cdots and 1:1 ratio of EDA:CA, and that of NG/Cdots(1:1,4)/Fe_3O_4 electrode was highest at 42 wt% of Fe_3O_4. Thus, NG75/PA/$Fe_3O_4$42 and NG/Cdots(1:1,4)/$Fe_3O_4$42 electrodes revealed the highest specific capacitance in each electrode series.

When the magnetic field of 8.98 mT was applied, the specific capacitance was enhanced for all electrodes: As recorded in Table 1, the calculated specific capacitance at scan rate of 5 mV/s under the magnetic fields of 0 mT and 8.98 mT, respectively, was 1064 F/g and 2001 F/g for NG75/PA/$Fe_3O_4$42 electrode and 1438 F/g and 2213 F/g for NG/Cdots(1:1,4)/$Fe_3O_4$42 electrode. Another characteristics of CV curves under the magnetic field is the less degradation of specific capacitance with increasing scan rate of NG/Cdots (x:1,4)/Fe_3O_4y (Fig. 7d and e). These behaviors were different from those of relevant electrodes without magnetic field and of NG75/PA/Fe_3O_4y with and without magnetic field. For instance, the specific capacitance of NG/Cdots(1:1,4)/$Fe_3O_4$42 electrode was 2213 F/g at 5 mV/s but still kept a value of 1286 F/g at 100 mV/s and 8.98 mT. Thus, Cdots component under the magnetic field affects for electrolytes to break loose from the behavioral restriction at electrolyte/electrode surface described above.

The GCD measurements were carried out on NG75/PA/$Fe_3O_4$42 and NG/Cdots(1:1,4)/$Fe_3O_4$42 electrodes under the magnetic fields of 0 and 8.98 mT at 1, 2, 4, and 6 A/g current densities. The GCD results illustrated in Fig. 8A were almost triangular curves without a serious potential drop, which frequently appears on the GCD of pseudocapacitor [41]. At all current densities, both the discharging time and the specific gravimetric capacitance were greater on the NG/Cdots(1:1,4)/$Fe_3O_4$42 electrode than on the NG75/PA/$Fe_3O_4$42

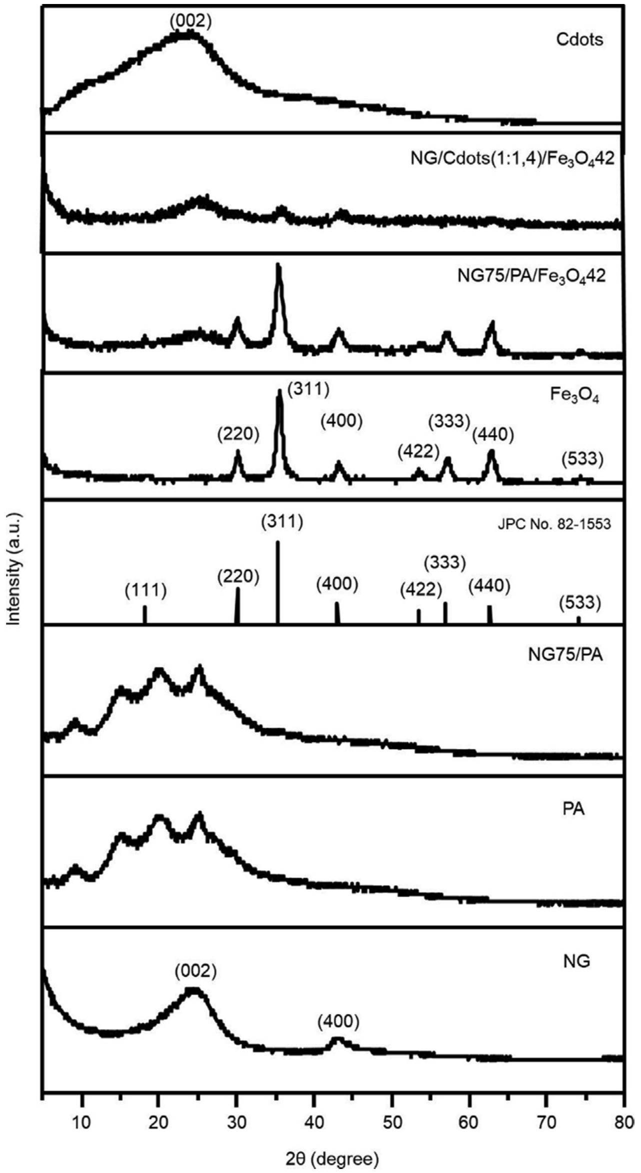

Fig. 3. XRD patterns of PA, NG75/PA, Fe_3O_4, NG75/PA/$Fe_3O_4$42, NG/Cdots(1:1,4)/$Fe_3O_4$42 and Cdots.

electrode and with the external magnetic field than without the field. Their numerical values at 1 A/g are listed in Table 1. This tendency was similar to CV behaviors.

Cycling stability is another critical factor in practical uses of supercapacitor electrode materials. The capacitance retention of NG75/PA/$Fe_3O_4$42 and NG/Cdots(1:1,4)/$Fe_3O_4$42, shown in Fig. 8B, was measured at 20 A/g (under normal condition) and 40 A/g (under a magnetic field of 8.98 mT) current densities. The NG75/PA/$Fe_3O_4$42 electrode retained only 81% after 2500 continuous cycles at the condition without a magnetic field, but the capacitance retention recovered to be 95% after adding a magnetic field of 8.98 mT. Whereas, the NG/Cdots(1:1,4)/$Fe_3O_4$42 electrode after 2500 cycles retained high retention (96%) both without/with the magnetic field, which is difficult from a case of NG75/PA/$Fe_3O_4$42 due to the difference of electrode stability by PA and Cdots. Thus, we further extend the measurement to 5000 cycles and confirmed the retension of 90% and 91%, respectively, without and with the magnetic field. The results indicate that the magnetic field is available to increase the retention or maintain high values. Under the magnetic field, both electrode materials started to increase retention above 100% at the beginning (about 500–1000) cycles, indicating that either the movement of ion or charge to the electrode/electrolyte interface increases the charge density around a double layer or the magnetic particles start inducing magnetization and then saturate. The stability of the present ternary composite electrodes besides the high specific capacitance can be attributed to the balanced amount of EDLC material (NG and Cdots) and pseudocapacitor material (PA and Fe_3O_4) in the composites. The presence of pseudocapacitor material exerts the high capacitance performance and the EDLC material acts in improving the electrochemical stability [41,42] of the composite electrodes. In fact, the NG75/PA/$Fe_3O_4$42 electrode is less stable than the NG/Cdots(1:1,4)/$Fe_3O_4$42 electrode. This difference may originate from the high content of the pseudocapacitor component in the former electrode.

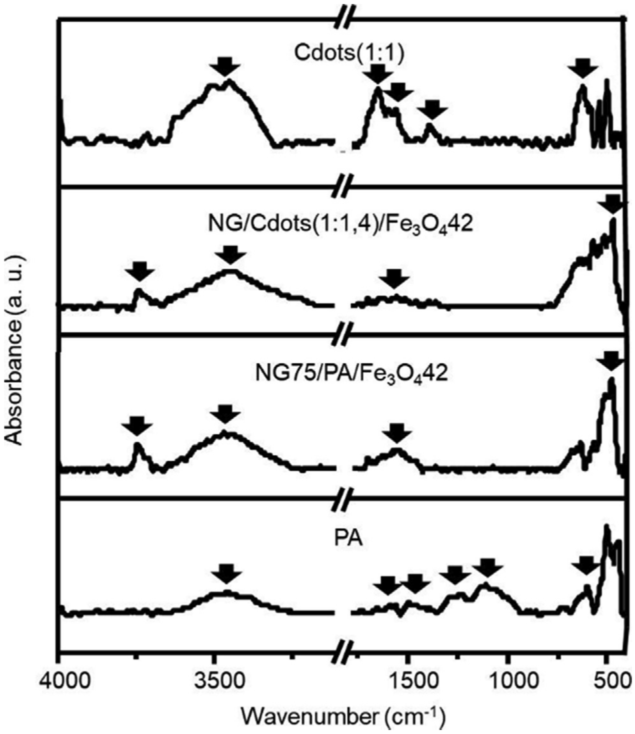

Fig. 4. FTIR absorption spectra of PA, NG75/PA/$Fe_3O_4$42, NG/Cdots(1:1,4)/$Fe_3O_4$42 and Cdots(1:1).

The specific energy density and the specific power density are important parameters to evaluate the electrode material. They were calculated based on the GCD results and shown in Fig. 8C. At the same specific power density (400 W/kg), the specific energy densities of NG/Cdots(1:1,4)/$Fe_3O_4$42 electrode (99.7 Wh/kg, and 143 Wh/kg at 0 mT and 8.98 mT, respectively) were higher than those of NG75/PA/$Fe_3O_4$42 electrode (54.1 Wh/kg and 96.2 Wh/kg at 0 mT and 8.98 mT, respectively) (see Table 2). Different scholars have investigated at different materials and conditions to evaluate the energy density and power density of supercapacitor as listed in Table 2. Although the reported energy density varied with electrodes, electrolytes and electrode systems, their energy and power densities at the conditions without applied magnetic field were comparable to the current results. However, it should be noted that the energy density under the magnetic field in the current work was higher than all results at the condition without magnetic field and a result from a magnetite/polypyrrole nanocomposite electrode under the magnetic field [23]. This phenomenon by the magnetic field can be caused by the induced

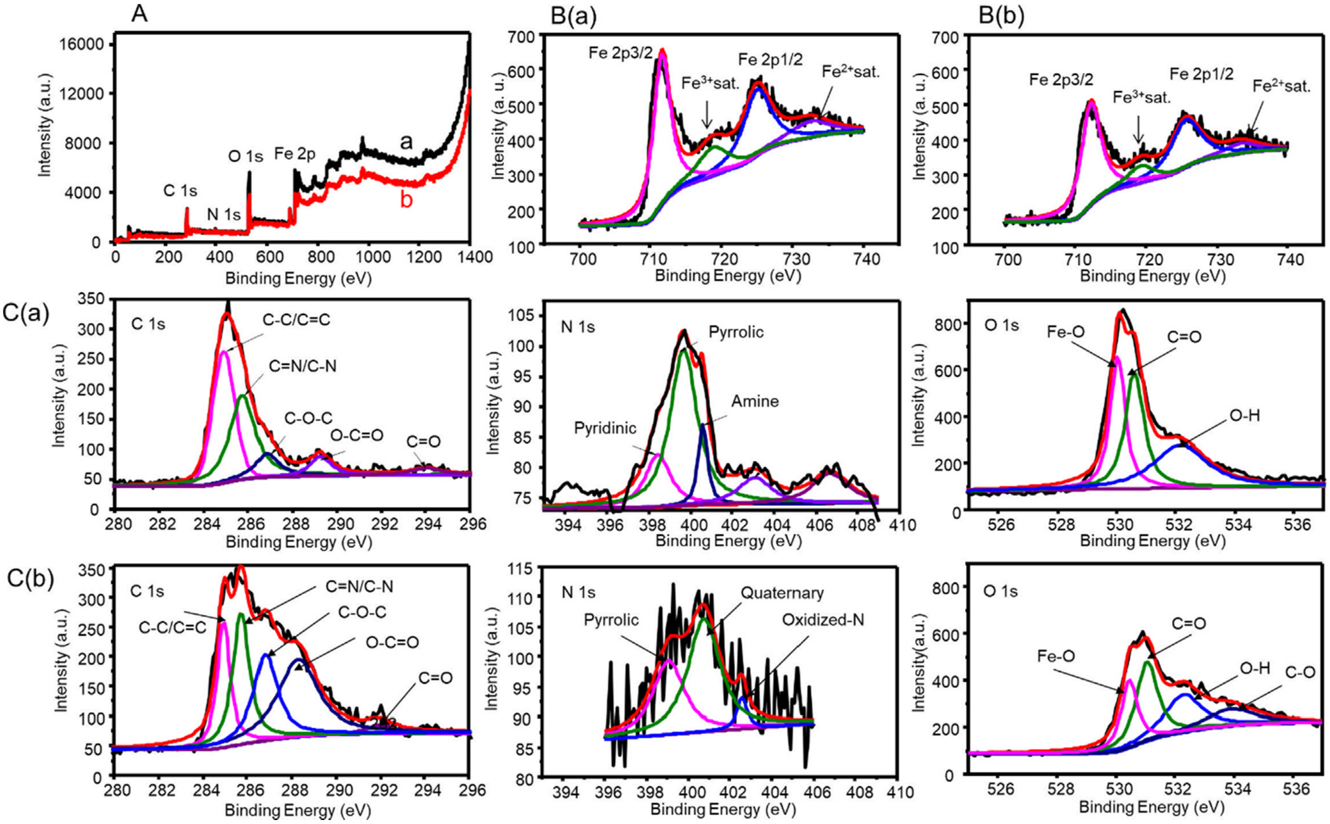

Fig. 5. XPS (A) survey spectra and fine and devonvoluted spectra of (B) Fe 2p, (C), C 1s, N 1s and O 1s of (a) NG75/PA/$Fe_3O_4$42 and (b) NG/Cdots(1:1,4)/$Fe_3O_4$42 nanocomposites.

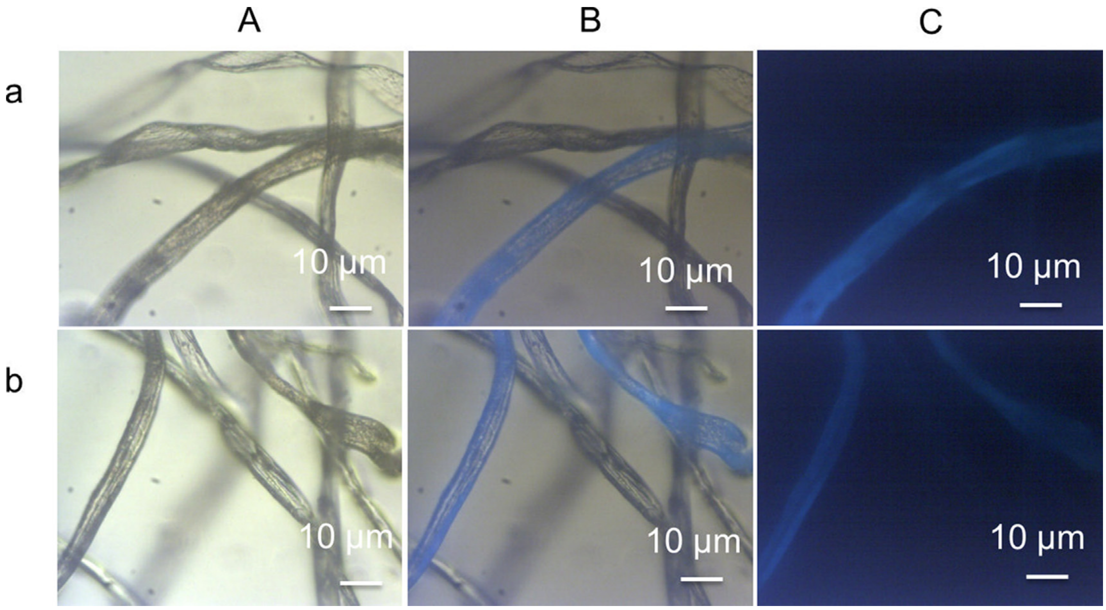

Fig. 6. (A) Optical, (B) merged (optical + fluorescence) and (C) fluorescence images of (a) Cdots(1:1) and (b) NG/Cdots(1:1,4) adsorbed on cotton fibers.

motion of the electrolyte ions to the electrode/electrolyte interface which reduces the resistance [23], increases their accessibility to an electrode surface, facilitates their movement, shortens their diffusion path length and accelerates their relaxation time due to the Lorentz effect.

Since the surface area of the electrode has a role of electron/ion capture and transfer, it should directly relate to the capacitance. The comparison between NG75/PA/$Fe_3O_4$42 and NG/Cdots(1:1,4)/$Fe_3O_4$42 composites was performed even on the nitrogen adsorption-desorption isotherm. As seen in Fig. 8D, the isotherms belong in the type IV curve with a hysteresis loop and are indicative of the presence of mesoporosity, which is an important indicator for the supercapacitor application of the as-prepared ternary composites. As listed in Table 1, the specific surface area and the

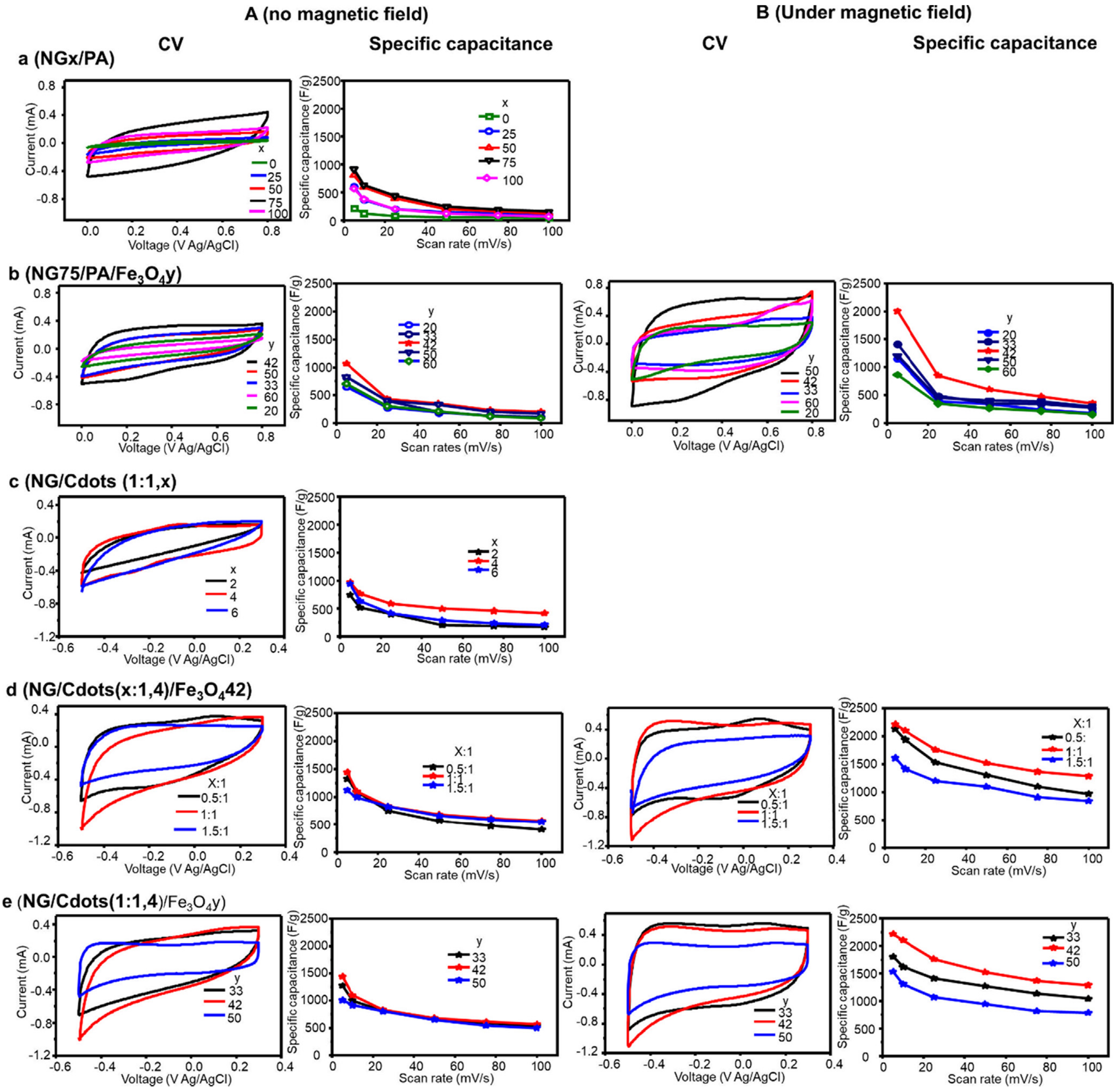

Fig. 7. CV curves at 5 mV/s scan rate and specific capacitance plots as a function of scan rate at the conditions (A) of no magnetic field and (B) under magnetic field (8.98 mT). (a) NGx/PA at different NG contents, (b) NG75/PA/Fe_3O_4y at different Fe_3O_4 contents, (c) NG/Cdots(1:1,x) at different Cdots contents, (d) NG/Cdots(x:1,4)/$Fe_3O_4$42 at different EDA:CA contents and (e) NG/Cdots(1:1,4)/Fe_3O_4y at different Fe_3O_4 contents.

pore volume of NG/Cdots(1:1,4)/$Fe_3O_4$42 were higher than those of NG75/PA/$Fe_3O_4$42, indicating the desirable adsorption of electrolyte ion on NG/Cdots(1:1,4)/$Fe_3O_4$42 electrode superior to NG75/PA/$Fe_3O_4$42 electrode. In comparison with the corresponding values (surface area of 213 m^2/g, pore volume of 0.263 cm^3/g, and pore diameter of 4.9 nm) of NG/Fe_3O_4 [11], the additive of PA or Cdots on NG/Fe_3O_4 unfavorably decreases the specific surface area and pore volume, although such effect was less by Cdots than by PA, and the pore diameter of NG75/PA/$Fe_3O_4$42 was largest due to the larger amount of PA (25 wt% in NG/PA) than that of Cdots (4 wt% in NG/Cdots). The size-limited Cdots (2–4 nm) [18] bring a less reduction of the surface area of the NG/Fe_3O_4 electrode and keep the accessible surface area and the interfacial polarization. Thus the NG/Cdots(1:1,4)/$Fe_3O_4$42 electrode has better capacitance properties and stability than NG75/PA/$Fe_3O_4$42.

In the presence of the stimulating field, the electrochemical performance of the composite electrode is improved, and the improvement should be connected with the increase of electron transfer efficiency at the electrolyte/electrode interface during an electrochemical measurement. The basic properties at such interface of NG75/PA/$Fe_3O_4$42 and NG/Cdots(1:1,4)/$Fe_3O_4$42 electrodes under the magnetic field can be inquired by an EIS in comparison with the condition without the external magnetic field. In the Nyquist plot shown in Fig. 9A, the electrode presented an arc and a straight line at higher and lower frequency regions, respectively, in both conditions without/with the external magnetic field, although the arc became smaller and the line became sharper under the magnetic field. The imaginary impedance axis reflects a pure capacitive behavior that represents the ion diffusion in the electrode material. The more straight the line, the more the

Table 1
A list of obtained parameters relating to NG75/PA/$Fe_3O_4$42 and NG/Cdots(1:1,4)/$Fe_3O_4$42 electrodes under the magnetic fields of 0 and 8.98 mT.

Electrode material	NG75/PA/$Fe_3O_4$42		NG/Cdots(1:1,4)/$Fe_3O_4$42	
Magnetic field (mT)	0	8.98	0	8.98
Specific capacitance (F/g) at 5 mV/s scan rate	1064	2001	1438	2213
Discharge time (*sec*) at 1 A/g current density	487	866	897	1287
Specific gravimetric capacitance (F/g) at 1 A/g current density	609	1083	1121	1609
Capacitance retention (%)	81	95	90	91
BET surface area (m^2/g)	87.96		189.4	
Total pore volume (cm^3/g)	0.143		0.225	
Mean pore diameter (nm)	6.5		4.8	
Solution resistance (Ω)	12	12	12	11
Warburg impedance ($\Omega.s^{-1/2}$)	174	40.6	37.8	23.6
Charge transfer resistance (Ω)	147	63	10	5
Relaxation time (μs)	600	350	566	6
Real impedance (*Ω*)	352.2	89.1	50.9	22.5
Imaginary impedance (*Ω*)	77.1	27.3	41.3	19.5
Real capacitance (*mF*)	1.0	5.2	15.3	36.9
Imaginary capacitance (*mF*)	4.5	17.1	18.9	40.7
a	2.5		2.9	
Q	2.2		2.2	
S	2.4		2.3	

supercapacitor behaves like an ideal capacitor, as seen under the magnetic field.

The solution resistance (Rs) and the charge transfer resistance (R_{ct}), based on a circuit drawn in the inset of Fig. 9A, were calculated from the real impedance intercept of the Nyquist plot [48], and numerical values were listed in Table 1. While the obtained solution resistance was similar even at different electrodes and the conditions without/with the external magnetic field, the charge transfer resistance of NG75/PA/$Fe_3O_4$42 electrode decreased from 147 to 63 Ω under the external magnetic field, it (10 Ω) of NG/Cdots(1:1,4)/$Fe_3O_4$42 electrode halved under the external magnetic field, and thus the charge transfer resistance was lower in NG/Cdots(1:1,4)/$Fe_3O_4$42 electrode than NG75/PA/$Fe_3O_4$42 electrode, referring to the more enhancement in electrical conductivity at electrode/electrolyte interface of NG/Cdots(1:1,4)/$Fe_3O_4$42 under the external magnetic field, because the charge transfer is accelerated.

The inclined portion of the curve in the middle frequency is assigned by Warburg impedance Ws [48,49], which is a consequence of the frequency dependence for ion diffusion/transport of the electrolyte to the electrode surface. As seen in Table 1, the Ws value of NG/Cdots(1:1,4)/$Fe_3O_4$42 was lower than that of NG75/PA/$Fe_3O_4$42 and it under the magnetic field was lower than it without the magnetic field. The lower value of Ws induces the access of electrolyte ions to the active electrode surface and indicates the greater variation in the ion diffusion path lengths and the decreased obstruction of ion movement [50], as happened under the magnetic field.

The relaxation time, which is the minimum time to discharge completely the energy from the electrode with an efficiency >50% [51], was observed from the Bode phase plot shown in Fig. 9B. The obtained values (see Table 1) were 600 and 350 μs for an NG75/PA/$Fe_3O_4$42 electrode and 566 and 6 μs for an NG/Cdots(1:1,4)/$Fe_3O_4$42 electrode at 0 and 8.98 mT, respectively. Thus the external magnetic field hastened the relaxation time, shortened the ionic transportation path lengths, led to lessen the internal resistance and increased the conductivity [51]. The ultra-fast electron transfer between NG and Fe_3O_4 in NG/Cdots(1:1)/$Fe_3O_4$42 electrode can happen preferably in Cdots-mediated composite electrode rather than in PA-mediated composite electrode.

Table 3 lists the reports of supercapacitor properties under different strengths of external magnetic fields. It indicated that the enhanced efficiency on capacitance varied depending on the magnetic field strength, the different nature and the loaded amount of the electroactive materials, the nature and amount of the electrolyte, and the experimental setup. It should be especially noticed that under the external magnetic field, the reported electrodes were more stable than under the normal condition due to the decreased obstruction of ion movement, the increased charge density around a double layer, and the induced magnetization.

3.3. Effects of external magnetic field on supercapacitor

Under the magnetic field, the integrated area of the CV curve increased, and hence the specific capacitance was enhanced as reported above (Fig. 7). It should have originated from the Lorentz effect, that is, due to the induction magnetization, the enhanced conductivity, and the increased charge density at the electrode/electrolyte interface, but its external magnetic field effect remains unclear. Thus, here we will focus on the enhancement mechanism of the specific capacitance on an NG/Cdots(1:1,4)/$Fe_3O_4$42 electrode under the external magnetic field and will develop a theoretical estimation to verify the effect of the external magnetic field on electrolyte/electrode interface via the complex impedance analyses in comparison between NG75/PA/$Fe_3O_4$42 and NG/Cdots(1:1,4)/$Fe_3O_4$42 electrodes.

The external magnetic field **B** generates a Lorentz force $\mathbf{F_L}$ in the solution, exerts a net drift velocity of the ions/charges, changes the transport rate of ions/charges in the electrochemical cell, and controls the diffusion of an electroactive species. Classical electromagnetism on the constituents of electrolytically accelerating ions/charges is described by a Lorentz force equation (Eq. (2)) [52];

$$\boldsymbol{F_L} = i \times B \tag{2}$$

where i is the current density. An electric current is proportional to the bulk electrolyte concentration C_{el} of the electroactive species. Thus the net driving force for supercapacitors under the magnetic field is proportional to both **B** and C_{el}.

If a current I_0 at 0 mT does not correlate with an increase in current ΔI_B generating under the magnetic field, that is, the current

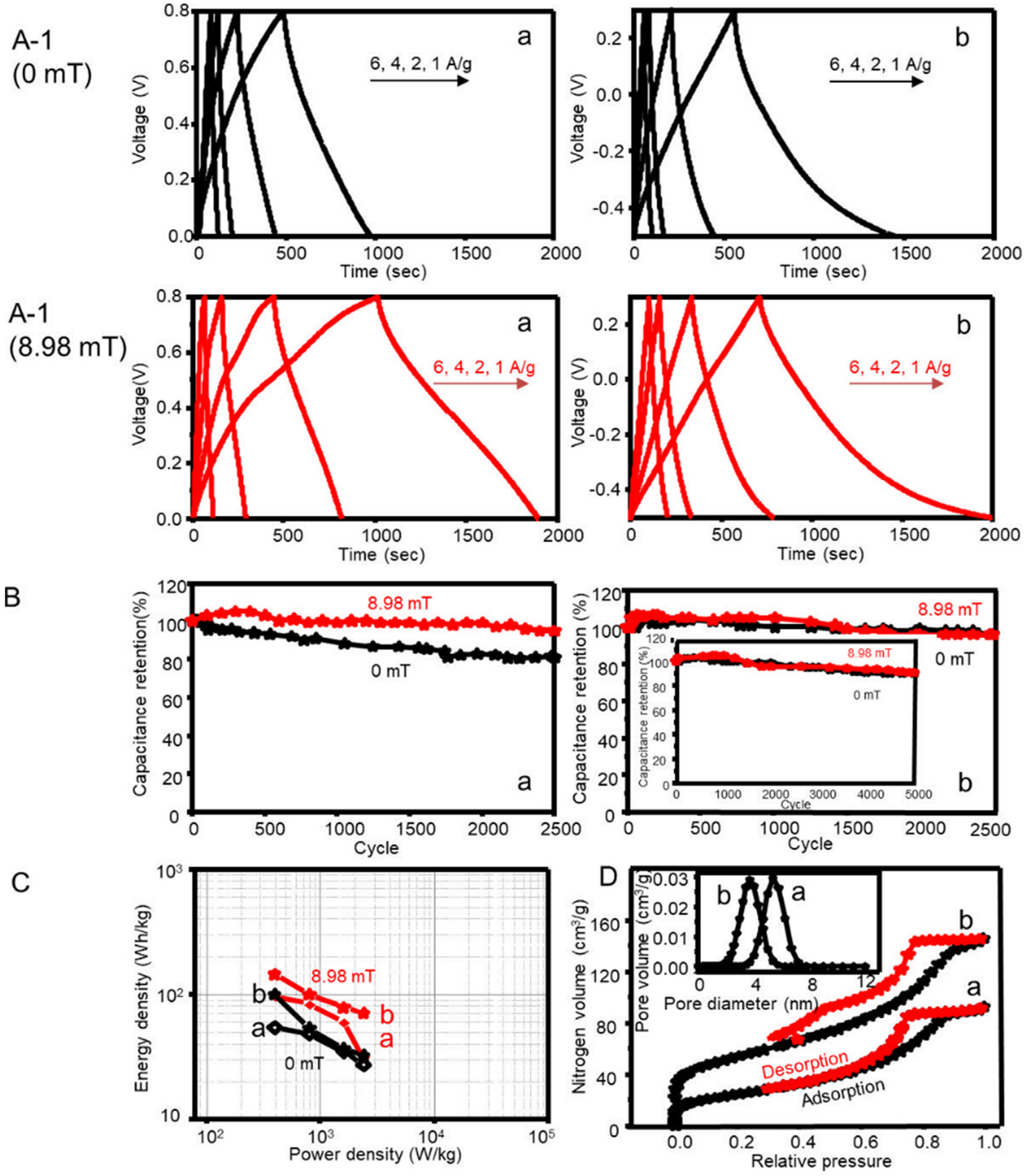

Fig. 8. (A) Charge-discharge profiles at 1, 2, 4, 6 A/g current densities under the magnetic fields of 0 and 8.98 mT, (B) capacitance retention profiles up to 2500 cycles at current densities of 20 A/g at 0 mT and 40 A/g at 8.98 mT, (C) Ragone plot at different current densities at 0 and 8.98 mT and (D) nitrogen adsorption-desorption isotherms. An inset in (Bb) is capacitance retention profiles up to 5000 cycles. An inset in (D) is pore diameter distributions. (a) NG/PA/$Fe_3O_4$42 and (b) NG/Cdots(1:1,4)/$Fe_3O_4$42.

under the magnetic field $I_B = I_0 + \Delta I_B$, the specific capacitance in Eq. (1a) can be rewritten by Eq. (3) under the magnetic field.

$$C_{S,B} = \int \frac{I_0}{m' v \Delta V} dV + \int \frac{\Delta I_B}{m' v \Delta V} dV = C_0 + \Delta C_B \tag{3}$$

Since C_0 is the specific capacitance in the absence of an external magnetic field, the net contribution of the magnetic field can be obtained by $C_{S,B}$-C_0, where ΔC_B is the increase in the specific capacitance depending on the magnetic field and an electrolyte. Based on the mass transport mechanism, Aaboubi, et al [52] have shown a relation of $\Delta I_B = kBC_{el}^{h}$, where k is a constant and h is an arbitrary power. On the other hand, Aogaki, et al. [53] have derived a relation of $\Delta I_B = k'B^{1/3}C_{el}^{4/3}$ under the different external magnetic fields and electrolyte concentrations. Thus, although ΔI_B or ΔC_B is probable to be a function of magnetic field and electrolyte concentration, their powers are obscure.

In the present work, the CV curves for an NG/Cdots(1:1,4)/$Fe_3O_4$42 electrode were measured at various bulk electrolyte concentrations and at conditions without/with magnetic field. The specific capacitance increased with bulk electrolyte concentration and was higher at 8.98 mT than at 0 mT, as seen in Fig. 10Aa. Then, the double logarithmic plot of $C_{S,B}$-Co versus C_{el} displayed a linear relation (see Fig. 10Ab) and the slope was 0.607 (=3/5). Thus, we obtained a relation of $\Delta C_B = k''B^{n'}C_{el}^{3/5}$ for an NG/Cdots(1:1,4)/$Fe_3O_4$42 electrode at 8.98 mT. The present experimental power of electrolyte concentration is fairly smaller than the power reported by Aogaki et al. [53]. The possibility of this difference may depend on the nature of electrolyte used, the cell design (distance between

Table 2
Comparison of specific energy density and power density from different supercapacitor electrode materials.

Electrode material*	Electrolyte*	Electrode system	Energy density (Wh/kg)		Power density (W/kg)		Ref.
			Without magnet	With magnet	Without magnet	With magnet	
rGO/Fe_3O_4/PA	PVA-H_3PO_4 gel	2	47.7		550		[15]
rGO/PA/eCFC	1 M H_2SO_4	2	25.4		52,500		[43]
MnO_2/rGO/AC	1 M H_2SO_4	2	119.3		500		[44]
GF-CNT@Fe_2O_3/GF-$CoMoO_4$	2 M KOH	2	74.7		1400		[45]
Nanostructured graphene/Fe_2O_3/PA	1 M KOH	3	107		351		[46]
rGO/molybdenum oxide/PA	1 M H_2SO_4	3	76.8		276.3		[47]
silica/PA	1 M H_2SO_4	3	37.4		430		[40]
Magnetite/Polypyrrole	1 M H_2SO_4	3	38.8	46.5	449.5	458.1	[23]
NG/PA/Fe_3O_4	1 M NaCl	3	54.1	96.2	400	400	This Work
NG/Cdots/Fe_3O_4	1 M NaCl	3	99.7	143.0	400	400	

[*] eCFC; nitrogen-doped carbon fiber cloth, AC; active carbon, GF-CNT; hierarchical graphite foam-carbon nanotube, GF-$CoMoO_4$; $CoMoO_4$ nanohoneycomb on graphite foam, PVA; poly-(vinyl alcohol).

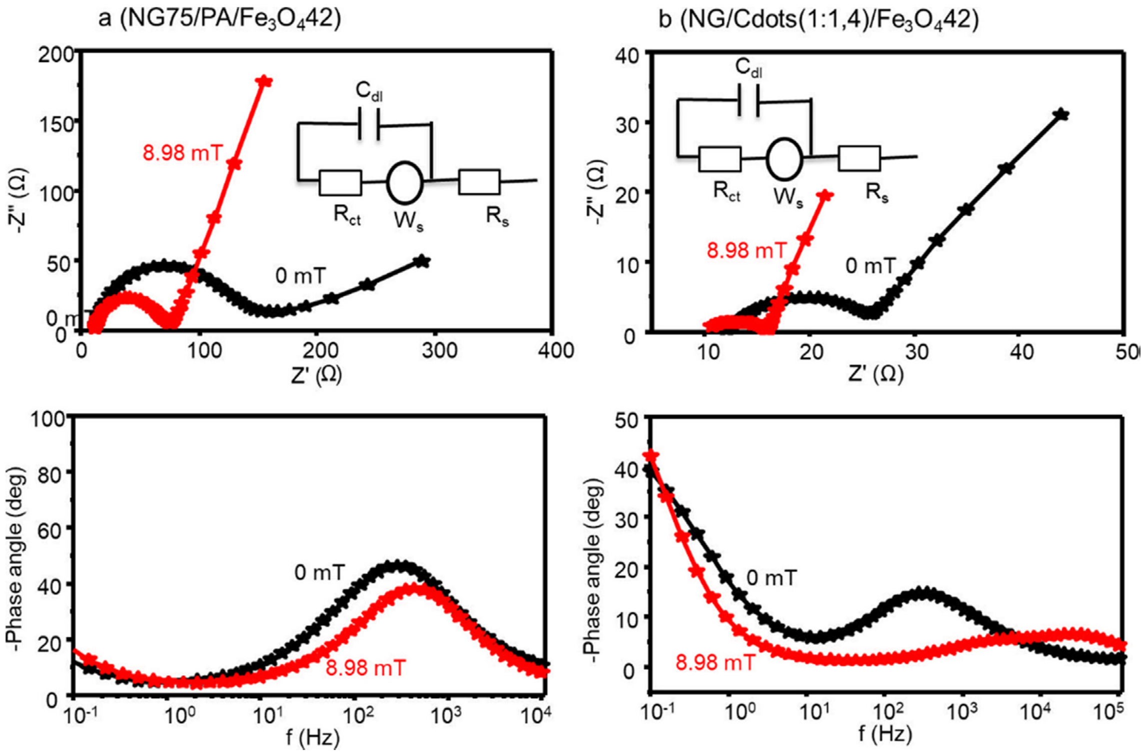

Fig. 9. (A) Nyquist plots and (B) Bode phase plots at frequency ranging from 100 kHz to 100 mHz at 10 mV amplitude of NG75/PA/$Fe_3O_4$42 and NG/Cdots(1:1,4)/$Fe_3O_4$42 electrodes at 0 and 8.98 mT magnetic fields. The fitted circuit is shown in inset of (A).

Table 3
Comparison of capacitance properties of different electrode/electrolyte systems under stimulated external magnetic fields.

Electrode material	Electrolyte	Specific capacitance at 5 mV/s (F/g)		Magnetic field	Stability (%) (cycle)		Ref.
		Without magnetic field	With magnetic field		Without magnetic field	With magnetic field	
Magnetic grapheme with Cdots	1 M NaCl	67	225	1191 G (119.1 mT)	–	95(9000)	[13]
Graphene	1 M Na_2SO_4	24.7(2 mV/s)	67.1%	720 G	84.2(500)	90.2(500)	[21]
Magnetic graphene		<10.7(2 mV/s)	154.6%(2 mV/s)	(72 mT)	96.1(500)	107.1(500)	
MnO_2	6 M KOH	119.2	141.7	1.34 mT	92.3(1000)	90(1000)	[4]
Active carbon/Fe_3O_4	6 M KOH	–	33.1%(1 A/g)	Micro strength	93.66(1000)	100(1000)	[24]
Fe_3O_4/NG	1 M NaCl	973	1254	8.98 mT	92(3000)	98(3000)	[11]
NiO/NG	1 M NaCl	697	747	8.98 mT	85(3000)		
Co_3O_4/NG	1 M NaCl	963	1092	8.98 mT	83(3000)		
NG/PA/Fe_3O_4	1 M NaCl	1064	2001	8.98 mT	81(2500)	95(2500)	This work
NG/Cdots/Fe_3O_4		1438	2213	8.98 mT	90(5000)	91(5000)	

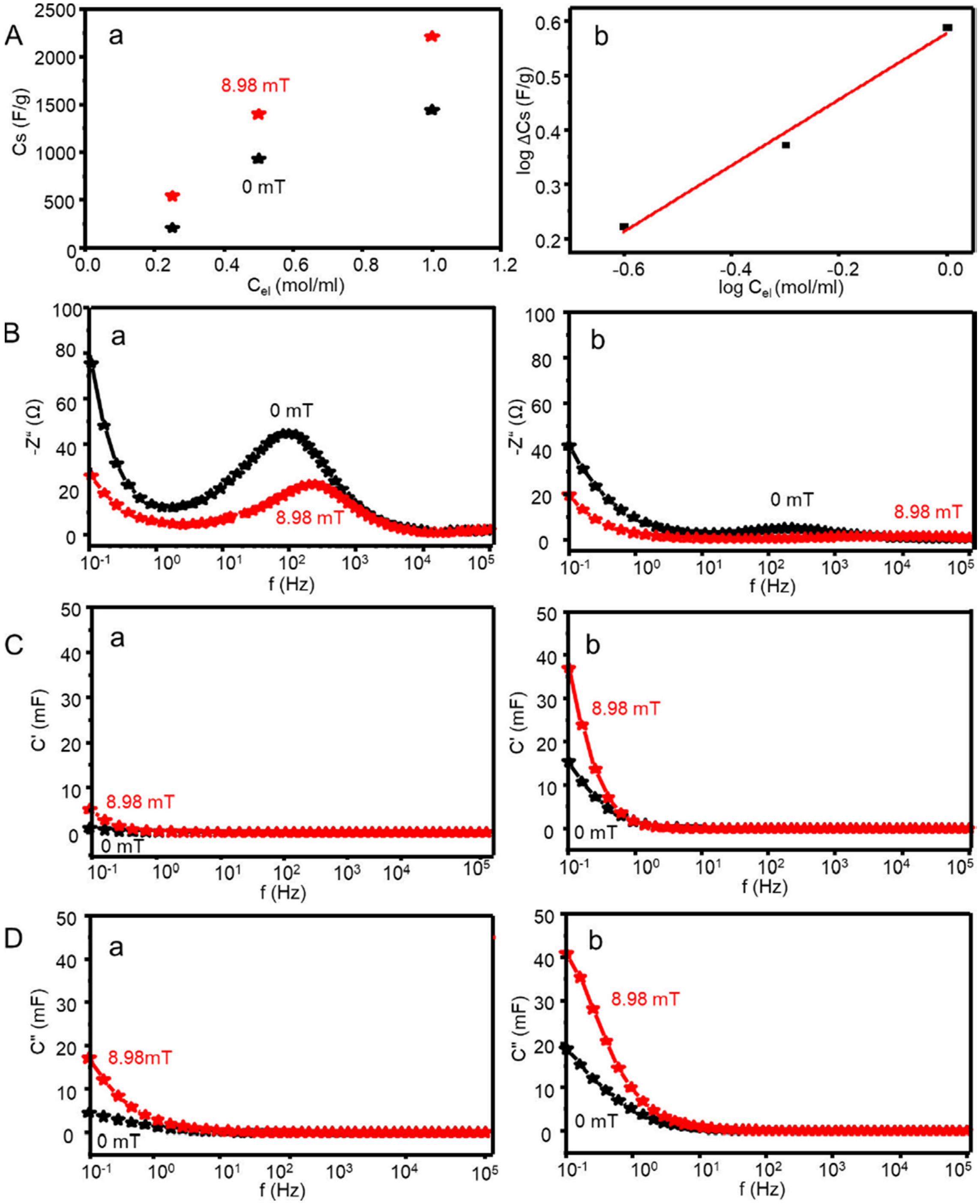

Fig. 10. (Aa) Specific capacitance values of an NG/Cdots(1:1,4)/$Fe_3O_4$42 electrode scanned at 5 mV/s as a function of electrolyte concentration under 0 and 8.98 mT magnetic fields, (Ab) the electrolyte concentration dependence of the increase in specific capacitance calculated from the results of (Aa). (B) Imaginary impedance and (C) real and (D) imaginary complex capacitances depending on frequency ranging from 100 kHz to 100 mHz at 10 mV amplitude under the external magnetic fields (0 and 8.98 mT). (a) NG75/PA/$Fe_3O_4$42 and (b) NG/Cdots(1:1,4)/$Fe_3O_4$42 electrodes.

electrodes), the strength of the magnetic field employed, the nature of an electroactive material, and the measurement system setup, but the additional trial will be requested to get any solution concerning to the power of electrolyte concentration.

The effect of the magnetic field on electrolyte/electrode interface was also examined by comparison of theoretical estimation with experimental results of the complex impedance analyses. Supposing that a redox reaction involving the oxidation O - reduction R process and the n electrons is given in Eq. (4) [54], which proceeds at the electrode surface in the electrolyte solution.

$$O + ne^- \rightleftharpoons R \tag{4}$$

For the high polarization, it can be assumed that the kinematics of ions can be enhanced due to the convective effect of Lorentz force. Then the kinetic equation m and m_B at the normal condition is given in Eq. (5a) [54].

$$m = m_0 e^{bV} \tag{5a}$$

In contrast, the kinetic equation m_B under the magnetic field can be written as Eq. (5b).

$$m_B = m_0 e^{b(1+B)V} \tag{5b}$$

where m_0 is an intrinsic kinetic constant, b = -$\alpha nF/RT$ for cathodic process, b = $\beta nF/RT$ for anodic process, V is an applied electric potential, F is an Faraday constant, and α and β are cathodic and anodic charge transfer coefficients, respectively. By means of the kinetic equation (Eq. (5)), the electric current equation $\left(I' = \pm \mathrm{nFA}m_p C_p(0,\mathrm{t})\right)$[54] can be given in Eq. (6a).

$$I' = nFAm_0 C_p(0,t)e^{bV} \tag{6a}$$

and the electric current equation under the magnetic field is written in the form of Eq. (6b).

$$I'_B = nFAm_0 C_p(0,t)e^{b(1+B)V} \tag{6b}$$

where p is O or R, A is an electrode area and $C_p(0,t)$ is the concentration of the species at the electrode surface at a position x = 0 and time t. Then, the ratio of electric currents with and without magnetic field is

$$\frac{I'_B}{I'} = e^{bBV} \tag{7}$$

Differentiating Eqs. (6a-b) with respect to the applied electric potential [54] and using Ohm's law gives Eqs. (8a-b).

$$\frac{\partial I'}{\partial V} = bI' = R_{ct}^{-1} \tag{8a}$$

$$\frac{\partial I'_B}{\partial V} = b(1+B)I'_B = R_{ctB}^{-1} \tag{8b}$$

Substitution of Eq. (8a) and Eq. (7) into Eq. (8b) results Eq. (9a).

$$R_{ct} = (1+B)R_{ctB}e^{bBV} \tag{9a}$$

Eq. (9a) indicates that $R_{ct} \gg R_{ctB}$, because b, B, and V are positive.

From Eq. (9a), we can rearrange for b in the form of Eq. (9b).

$$b = \frac{1}{VB}\left[\ln\left(\frac{R_{ct}}{R_{ctB}}\right) - \ln(1+B)\right] \tag{9b}$$

The evaluated experimental values (see Table 1) of the charge transfer resistance at 0 and 8.98 mT, respectively, are 147 and 63 Ω for an NG75/PA/$Fe_3O_4$42 electrode and 10 and 5 Ω for an NG/Cdots(1:1,4)/$Fe_3O_4$42 electrode, indicating that the charge transfer resistance is reduced under the external magnetic field and hence an electric current and a conductivity are raised, as theoretically estimated above. The open circuit voltage is 0.286 V and the applied magnetic field is 0.00898 T. Thus the calculated value of b is 266.4 and 326.4 V^{-1} T^{-2} for NG/Cdots(1:1,4)/$Fe_3O_4$42 and NG75/PA/$Fe_3O_4$42, respectively.

The EIS is a tool to measure the frequency-based impedance of the electrode/electrolyte interface. An electrochemical electrode/-electrolyte interface consists of capacitor and resistor components integrated into a simple circuit. When a small amplitude sinusoidal alternating current of 10 mV is applied on an EIS measurement, the resulting sinusoidal voltage V(t) and current I(t) at a time t are helpful to define the complex impedance Z(ω) [55–57].

$$Z_0 = V(t)/I(t) = Z'_0 + jZ''_0 \tag{10a}$$

Then, against the general relation (Eq. (10a)), the complex impedance $Z_B(\omega)$ under the magnetic field must be described as

$$Z_B = V_B/I_B = Z'_B + jZ''_B = Z'_0 - \Delta Z'_B + j(Z''_0 - \Delta Z''_B) \tag{10b}$$

where Z'_0 and Z''_0 are the real and imaginary impedance, respectively, at 0 mT, $\Delta Z'_B$ and $\Delta Z''_B$ are the change in real and imaginary impedance, respectively, under the magnetic field and j is a complex number.

In association with the processes at the electrode/electrolyte interface, the double-layer capacitance C_{dl} associated with the imaginary impedance [56] can be calculated from Eqs. (11a) and (11b) for the processes without and with the external magnetic field, respectively.

$$C_{dl0} = \frac{-1}{2\pi f Z''_0} \tag{11a}$$

$$C_{dlB} = C_{dl0} + \Delta C_{dlB} = \frac{-1}{2\pi f}\left[\frac{1}{Z''_0} + \frac{1}{\Delta Z''_B}\right] \tag{11b}$$

By using $Eq\ (11a)\ and\ \Delta Z''_B \equiv Z''_0 - Z''_B$ (see Eq. (10b)), Eq. (11b) becomes

$$C_{dlB} = Z''_0 C_{dl0}\left[\frac{1}{Z''_0} + \frac{1}{Z''_0 - Z''_B}\right] = C_{dl0}\frac{2Z''_0 - Z''_B}{Z''_0 - Z''_B} \tag{12}$$

$$C_{dlB} = aC_{dl0} \tag{13}$$

where a = $\frac{2-\frac{Z''_B}{Z''_0}}{1-\frac{Z''_B}{Z''_0}}$

It is evident from Fig. 10B that $Z''_0 > Z''_B$ for both NG75/PA/$Fe_3O_4$42 (77.1 > 27.3 Ω) and NG/Cdots(1:1,4)/$Fe_3O_4$42 (41.3 > 19.5 Ω) at 100 mHz. The calculated value of a is 2.5 and 2.9 for NG75/PA/$Fe_3O_4$42 and NG/Cdots(1:1,4)/$Fe_3O_4$42, respectively, (see Table 1), indicating that the double-layer capacitance at a certain frequency under the magnetic field is higher than under the normal condition.

The complex capacitance is used to relate the specific capacitance to the frequency. The electrochemical capacitance can be expressed by a real part C' and an imaginary part C'' defined in Eq. (14) [55]. The real part is the electrode capacitance measured during constant discharge current at low frequency and the imaginary part corresponds to the energy dissipation process.

$$C = C' - jC'' = 1/j\omega Z \tag{14}$$

Substitution of Eq. (10a) in Eq. (14) and rationalization yield Eq. (15).

$$C = C' - jC'' = -\frac{Z''_0}{\omega|Z_0|^2} + \frac{Z'_0}{j\omega|Z_0|^2} \tag{15}$$

From Eq. (15), we can separate C'_0 and C''_0 into Eqs. (16a, b).

$$C'_0 = -\frac{Z''_0}{\omega|Z_0|^2}\ or\ C'_0|Z_0|^2 = -\frac{Z''_0}{\omega} \tag{16a}$$

$$C''_0 = \frac{Z'_0}{\omega|Z_0|^2}\ or\ C''_0|Z_0|^2 = \frac{Z'_0}{\omega} \tag{16b}$$

Defining the change in complex capacitance under the magnetic field using the relation $\Delta Z_B \equiv Z_0 - Z_B$, $\Delta C'_B$ and $\Delta C''_B$ are given by Eqs. (16c, d)

$$\Delta C'_B = -\frac{Z''_0 - Z''_B}{\omega|Z_0 - Z_B|^2} \tag{16c}$$

$$\Delta C''_B = \frac{Z'_0 - Z'_B}{\omega|Z_0 - Z_B|^2} \tag{16d}$$

and the complex capacitance under the magnetic field can be given in Eq. (16e).

$$C_B = C_0 + \Delta C_B = (C'_0 + \Delta C'_B) - j(C''_0 + \Delta C''_B) \tag{16e}$$

When Eqs. (16c, d) are used, the real and imaginary capacitances under the magnetic field from Eq. (16e) is given in Eqs. (16f, g).

$$C'_B = -\frac{Z''_0}{\omega}\left(\frac{1}{|Z_0|^2} + \frac{1 - Z''_{\boldsymbol{B}}/Z''_0}{|Z_0 - Z_B|^2}\right) \quad (16f)$$

$$C''_B = \frac{Z\prime_0}{\omega}\left(\frac{1}{|Z_0|^2} + \frac{1 - Z'_{\boldsymbol{B}}/Z'_0}{|Z_0 - Z_B|^2}\right) \quad (16g)$$

Substituting Eqs. (16a, b) into Eqs (16f, g) results Eqs. (16h, i).

$$C'_B = QC'_0 \quad (16h)$$

$$C''_B = SC''_0 \quad (16i)$$

where Q = $1 + (1 - Z''_{\boldsymbol{B}}/Z''_0)\left(\frac{|Z_0|^2}{|Z_0 - Z_B|^2}\right)$, S = $1 + (1 - Z'_{\boldsymbol{B}}/Z'_0)\left(\frac{|Z_0|^2}{|Z_0 - Z_B|^2}\right)$, $|Z_0|^2 = {Z'_0}^2 + {Z''_0}^2$, and $|Z_0 - Z_B|^2 = (Z'_0 - Z'_B)^2 + (Z''_0 - Z''_B)^2$.

The spectral distribution of real and imaginary capacitance versus frequency of NG75/PA/$Fe_3O_4$42 and NG/Cdots(1:1,4)/$Fe_3O_4$42 electrodes is shown in Fig. 10C and D. The spectral distribution decreased with increasing frequency within the wide range of 100 mHz to 100 kHz measured under the external magnetic field (0 and 8.98 mT). Then, the capacitance was highest at the lowest frequency (100 mHz), but it behaved like a pure resistor in the higher frequency region, because the spectral distribution in these regions is nearly insignificant in the specific capacitance. The calculated values of Q and S were 2.2 and 2.4 for NG75/PA/$Fe_3O_4$42 and 2.2 and 2.3 for NG/Cdots(1:1,4)/$Fe_3O_4$42 electrodes at 0 and 8.98 mT, respectively, as listed in Table 1. These values indicate that both Q and S are positive values. Similarly, the experimental values of $C', C'_B, C'', \mathit{and}\ C''_B$, given in Table 1, respectively, were 1.0, 5.2, 4.5 and 17.1 mF for an NG75/PA/$Fe_3O_4$42 electrode and 15.3, 36.9, 18.9 and 40.7 mF for an NG/Cdots(1:1,4)/$Fe_3O_4$42 electrode. These data reveal that the complex capacitance was higher under the magnetic field than at the normal condition.

Based on the Lorentz force theory and the CV measurement at different electrolyte concentrations, it was found that the increase of the specific capacitance for an NG/Cdots(1:1,4)/$Fe_3O_4$42 electrode at constant magnetic field was proportional to the electrolyte concentration in the power of 3/5 ($C_{el}^{3/5}$). The Lorentz effect in the presence of a magnetic field can accelerate the moving of charges/ions to the electrode/electrolyte interface and hence can induce the convection of electrolytes. The induced convection can reduce the charge transfer resistance, increase the charge density at the electrode/electrolyte interface and enhance almost doubly the double-layer capacitance as well as complex capacitance under the magnetic field. These theoretical assumptions were proved in comparison with the experimental results obtained via the complex impedance measurements, and it was confirmed that an NG/Cdots(1:1,4)/$Fe_3O_4$42 electrode was better effective than an NG75/PA/$Fe_3O_4$42 electrode in good agreement with CV and GCD experimental results.

4. Conclusions

In summary, we have successfully synthesized NG/PA/Fe_3O_4 and NG/Cdots/Fe_3O_4 ternary composites for the supercapacitor. The in situ synthesis method showed the best route to incorporate the conductive materials and magnetic metal oxide. When the eletrochemical properties of the present electrodes were compared with those of NG/Fe_3O_4 electrode previously reported [11], it is obvious that the addition of PA or Cdots on NG/Fe_3O_4 nanocomposites, in common, increased the conductivity, reduced the charge transfer resistance, accelerated the relaxation time, facilitated the charge transfer, and enhanced the specific capacitance. However, the difference on electrochemical response between NG/PA/Fe_3O_4 and NG/Cdots/Fe_3O_4, which was revealed in the present research, may depend on the structural and characteristic differences between two electrode materials, because highly conductive PA takes an 1D structure (nanowire) and less conductive Cdot does a 0D structure (nanodot). An NG/Cdots/Fe_3O_4 electrode have shown superior capacitance and specific energy density to an NG/PA/Fe_3O_4 electrode due to ultra-fast electron donor/acceptor properties owing to small sized Cdots. Nevertheless, the external magnetic field has enhanced the specific capacitance and the stability of both hybrid electrodes.

Especially, the addition of an external magnetic field has resulted in a magnetic induction that arises a convection or a concentration modification of the electrolyte at the electrolyte/electrode interface and a variation of the resistances of electrodes. Then the specific capacitance proportional to the bulk electrolyte concentration with a power of 3/5 ($C_{el}^{3/5}$) has been derived at a constant external magnetic field for an NG/Cdots(1:1,4)/$Fe_3O_4$42 electrode and such relation may depend on the experimental conditions but the further prospect is requisite. The complex impedance analyses have provided the reduced charge transfer resistance, the enhanced electrical conductivity, and hence the increased double-layer capacitance. The complex capacitance has almost doubled under the magnetic field due to the convection induced by the Lorentz force. Such relation has been confirmed based on the theoretical estimation. The present results will open a new window for the clarification of the enhancement mechanisms on capacitance efficiency under the external magnetic field.

Declaration of Competing Interest

The authors declare that they have no known competing financial interests or personal relationships that could have appeared to influence the work reported in this paper.

Acknowledgements

This research was partially supported by the Ministry of Science and Technology, Taiwan (MOST 108-2221-E-011-105-). M.C.F. gratefully acknowledges National Taiwan University of Science and Technology, Taiwan, for the financial support by student scholarship. We thank Prof. H. Ohshima, Tokyo University of Science, Japan, for his valuable comments in association with the effect of magnetic field. We give thanks to Prof. L.-C. Chao, National Taiwan University of Science and Technology, for his kind permission to use a DC power supply instrument.

References

[1] B.M. Fronk, R. Neal, S. Garimella, Evolution of the transition to a world driven by renewable energy, J. Energy Resour. Technol. 132 (2) (2010), https://doi.org/10.1115/1.4001574 021009.

[2] O. Ellabban, H. Abu-Rub, F. Blaabjerg, Renewable energy resources: Current status, future prospects and their enabling technology, Renew. Sust. Energ. Rev. 39 (2014) 748–764, https://doi.org/10.1016/j.rser.2014.07.113.

[3] C. Du, J. Yeh, N. Pan, High power density supercapacitors using locally aligned carbon nanotube electrodes, Nanotechnology 16 (4) (2005) 350–353, https://doi.org/10.1088/0957-4484/16/4/003.

[4] Z. Zeng, Y. Liu, W. Zhang, H. Chevva, J. Wei, Improved supercapacitor performance of MnO_2-electrospun carbon nanofibers electrodes by mT magnetic field, J. Power Sources 358 (2017) 22–28, https://doi.org/10.1016/j.jpowsour.2017.05.008.

[5] P. Hiralal, H. Wang, H.E. Unalan, Y. Liu, M. Rouvala, D. Wei, P. Andrew, G.A. Amaratunga, Enhanced supercapacitors from hierarchical carbon nanotube and nanohorn architectures, J. Mater. Chem. 21 (44) (2011) 17810–17815, https://doi.org/10.1039/C1JM12156A.

[6] P. Simon, Y. Gogotsi, Materials for electrochemical capacitors, in: Nanoscience and technology: a collection of reviews from Nature journals, World Scientific, 2010, pp. 320–329. https://doi.org/10.1142/9789814287005_0033.

[7] L.L. Zhang, X. Zhao, Carbon-based materials as supercapacitor electrodes, Chem. Soc. Rev. 38 (9) (2009) 2520–2531, https://doi.org/10.1039/B813846J.

[8] Y.-G. Wang, H.-Q. Li, Y.-Y. Xia, Ordered whiskerlike polyaniline grown on the surface of mesoporous carbon and its electrochemical capacitance performance, Adv. Mater. 18 (19) (2006) 2619–2623, https://doi.org/10.1002/adma.200600445.

[9] R.R. Salunkhe, S.-H. Hsu, K.C. Wu, Y. Yamauchi, Large-scale synthesis of reduced graphene oxides with uniformly coated polyaniline for supercapacitor applications, ChemSusChem 7 (6) (2014) 1551–1556, https://doi.org/10.1002/cssc.201400147.

[10] X. Yan, Y. Wang, Z. Ma, Synthesis, characterization and electrochemical performance of cobalt oxides for supercapacitor, Int. J. Electrochem. Sci. 13 (2018) 1074–1083, https://doi.org/10.20964/2018.01.87.

[11] M.C. Fite, J.-Y. Rao, T. Imae, Effect of external magnetic field on hybrid supercapacitors of nitrogen-doped graphene with magnetic metal oxides, Bull. Chem. Soc. Jpn. 93 (9) (2020) 1139–1149, https://doi.org/10.1246/bcsj.20200128.

[12] C.C. Chang, T. Imae, Synergistic performance of composite supercapacitors between carbon nanohorn and conducting polymer, ACS Sustain. Chem. Eng. 6 (4) (2018) 5162–5172, https://doi.org/10.1021/acssuschemeng.7b04813.

[13] M.M.M. Ahmed, T. Imae, Effect of external magnetic field on cyclic voltammetry of exfoliated graphene-based magnetic composites with conductive polymer and carbon dots, J. Magn. Magn. Mater. 491 (2019), https://doi.org/10.1016/j.jmmm.2019.165604 165604.

[14] M.M.M. Ahmed, T. Imae, Electrochemical properties of a thermally expanded magnetic graphene composite with a conductive polymer, PCCP 18 (15) (2016) 10400–10410, https://doi.org/10.1039/c6cp00311g.

[15] S. Mondal, U. Rana, S. Malik, Reduced graphene oxide/Fe_3O_4/polyaniline nanostructures as electrode materials for an all-solid-state hybrid supercapacitor, J. Phys. Chem. C 121 (14) (2017) 7573–7583, https://doi.org/10.1021/acs.jpcc.6b10978.

[16] P. Yu, X. Wen, Y.-R. Toh, Y.-C. Lee, K.-Y. Huang, S. Huang, S. Shrestha, G. Conibeer, J. Tang, Efficient electron transfer in carbon nanodot–graphene oxide nanocomposites, J. Mater. Chem. C 2 (16) (2014) 2894–2901, https://doi.org/10.1039/C3TC32395A.

[17] M. Tuerhong, X. Yang, Y. Xue-Bo, Review on carbon dots and their applications, Chin. J. Anal. Chem. 45 (1) (2017) 139–150, https://doi.org/10.1016/S1872-2040(16)60990-8.

[18] H.F. Etefa, T. Imae, M. Yanagida, Enhanced photosensitization by carbon dots co-adsorbing with dye on p-type semiconductor (nickel oxide) solar cells, ACS Appl. Mater. Interfaces 12 (16) (2020) 18596–18608, https://doi.org/10.1021/acsami.0c02413.

[19] W. Liu, C. Li, Y. Ren, X. Sun, W. Pan, Y. Li, J. Wang, W. Wang, Carbon dots: surface engineering and applications, J. Mater. Chem. B 4 (35) (2016) 5772–5788, https://doi.org/10.1039/C6TB00976J.

[20] B. Unnikrishnan, C.-W. Wu, I.-W.-P. Chen, H.-T. Chang, C.-H. Lin, C.-C. Huang, Carbon dot-mediated synthesis of manganese oxide decorated graphene nanosheets for supercapacitor application, ACS Sustain. Chem. Eng. 4 (6) (2016) 3008–3016, https://doi.org/10.1021/acssuschemeng.5b01700.

[21] J. Zhu, M. Chen, H. Qu, Z. Luo, S. Wu, H.A. Colorado, S. Wei, Z. Guo, Magnetic field induced capacitance enhancement in graphene and magnetic graphene nanocomposites, Energy Environ. Sci. 6 (1) (2013) 194–204, https://doi.org/10.1039/C2EE23422J.

[22] G. Bin, H.-B. Han, C. Feng, Influence of magnetic field on microstructural and dynamic properties of sodium, magnesium and calcium ions, Trans. Nonferrous Met. Soc. China 21 (2011) s494–s498, https://doi.org/10.1016/S1003-6326(11)61631-2.

[23] H. Wei, H. Gu, J. Guo, D. Cui, X. Yan, J. Liu, D. Cao, X. Wang, S. Wei, Z. Guo, Significantly enhanced energy density of magnetite/polypyrrole nanocomposite capacitors at high rates by low magnetic fields, Adv. Compos. Hybrid Mater. 1 (1) (2018) 127–134, https://doi.org/10.1007/s42114-017-0003-4.

[24] G. Wang, H. Xu, L. Lu, H. Zhao, Magnetization-induced double-layer capacitance enhancement in active carbon/Fe_3O_4 nanocomposites, J. Energy Chem. 23 (6) (2014) 809–815, https://doi.org/10.1016/S2095-4956(14)60216-3.

[25] S. Pal, S. Majumder, S. Dutta, S. Banerjee, B. Satpati, S. De, Magnetic field induced electrochemical performance enhancement in reduced graphene oxide anchored Fe_3O_4 nanoparticle hybrid based supercapacitor, J. Phys. D Appl. Phys. 51 (37) (2018), https://doi.org/10.1088/1361-6463/aad5b3 375501.

[26] C.C. Chang, T.A. Geleta, T. Imae, Effect of carbon dots on supercapacitor performance of carbon nanohorn/conducting polymer composites, Bull. Chem. Soc. Jpn. (2020), https://doi.org/10.1246/bcsj.20200269.

[27] M.T. Efa, T. Imae, Hybridization of carbon-dots with ZnO nanoparticles of different sizes, J. Taiwan Inst. Chem. Eng. 92 (2018) 112–117, https://doi.org/10.1016/j.jtice.2018.02.007.

[28] M.M.M. Ahmed, T. Imae, J.P. Hill, Y. Yamauchi, K. Ariga, L.K. Shrestha, Defect-free exfoliation of graphene at ultra-high temperature, Colloids Surf. A Physicochem. Eng. Asp. 538 (2018) 127–132, https://doi.org/10.1016/j.colsurfa.2017.10.074.

[29] T.T. Debelo, M. Ujihara, Effect of simultaneous electrochemical deposition of manganese hydroxide and polypyrrole on structure and capacitive behavior, J. Electroanal. Chem. 113825 (2020), https://doi.org/10.1016/j.jelechem.2020.113825.

[30] H. Nie, M. Li, Q. Li, S. Liang, Y. Tan, L. Sheng, W. Shi, S.-X.-A. Zhang, Carbon dots with continuously tunable full-color emission and their application in ratiometric pH sensing, Chem. Mater. 26 (10) (2014) 3104–3112, https://doi.org/10.1021/cm5003669.

[31] K. Bhattacharya, P. Deb, Hybrid nanostructured C-dot decorated Fe_3O_4 electrode materials for superior electrochemical energy storage performance, Dalton Trans. 44 (19) (2015) 9221–9229, https://doi.org/10.1039/c5dt00296f.

[32] T.-M. Wu, Y.-W. Lin, C.-S. Liao, Preparation and characterization of polyaniline/multi-walled carbon nanotube composites, Carbon 43 (4) (2005) 734–740, https://doi.org/10.1016/j.carbon.2004.10.043.

[33] A. Allen, C. Senoff, Infrared spectra of tris-ethylenediamine complexes of Ruthenium (II), Can. J. Chem. 43 (4) (1965) 888–895, https://doi.org/10.1139/v65-115.

[34] M.C. Bautista, O. Bomati-Miguel, M. del Puerto Morales, C.J. Serna, S. Veintemillas-Verdaguer, Surface characterisation of dextran-coated iron oxide nanoparticles prepared by laser pyrolysis and coprecipitation, J. Magn. Magn. Mater. 293 (1) (2005) 20–27, https://doi.org/10.1016/j.jmmm.2005.01.038.

[35] T.M. de Lima Alves, B.F. Amorim, M.A.M. Torres, C.G. Bezerra, S.N. de Medeiros, P.L. Gastelois, L.E.F. Outon, W.A. de Almeida Macedo, Wasp-waisted behavior in magnetic hysteresis curves of $CoFe_2O_4$ nanopowder at a low temperature: experimental evidence and theoretical approach, RSC Adv. 7 (36) (2017) 22187–22196, https://doi.org/10.1039/C6RA28727A.

[36] T.-C. Lin, G. Seshadri, J.A. Kelber, A consistent method for quantitative XPS peak analysis of thin oxide films on clean polycrystalline iron surfaces, Appl. Surf. Sci. 119 (1–2) (1997) 83–92, https://doi.org/10.1016/S0169-4332(97)00167-0.

[37] H.R. Tantawy, B.-A.-F. Kengne, D.N. McIlroy, T. Nguyen, D. Heo, Y. Qiang, D.E. Aston, X-ray photoelectron spectroscopy analysis for the chemical impact of solvent addition rate on electromagnetic shielding effectiveness of HCl-doped polyaniline nanopowders, J. Appl. Phys. 118 (17) (2015), https://doi.org/10.1063/1.4934851 175501.

[38] D. Wang, T. Imae, M. Miki, Fluorescence emission from PAMAM and PPI dendrimers, J. Colloid Interface Sci. 306 (2) (2007) 222–227, https://doi.org/10.1016/S0021-9797(07)00550-4.

[39] S. Shahrokhian, R. Mohammadi, E. Asadian, One-step fabrication of electrochemically reduced graphene oxide/nickel oxide composite for binder-free supercapacitors, Int. J. Hydrog. Energy 41 (39) (2016) 17496–17505, https://doi.org/10.1016/j.ijhydene.2016.07.087.

[40] H. Wei, H. Gu, J. Guo, S. Wei, J. Liu, Z. Guo, Silica doped nanopolyaniline with endured electrochemical energy storage and the magnetic field effects, J. Phys. Chem. C 117 (25) (2013) 13000–13010, https://doi.org/10.1021/jp403656q.

[41] B. Devadas, T. Imae, Effect of carbon dots on conducting polymers for energy storage applications, ACS Sustain. Chem. Eng. 6 (1) (2018) 127–134, https://doi.org/10.1021/acssuschemeng.7b01858.

[42] P. Xiong, H. Huang, X. Wang, Design and synthesis of ternary cobalt ferrite/graphene/polyaniline hierarchical nanocomposites for high-performance supercapacitors, J. Power Sources 245 (2014) 937–946, https://doi.org/10.1016/j.jpowsour.2013.07.064.

[43] P. Yu, Y. Li, X. Zhao, L. Wu, Q. Zhang, Graphene-wrapped polyaniline nanowire arrays on nitrogen-doped carbon fabric as novel flexible hybrid electrode materials for high-performance supercapacitor, Langmuir 30 (18) (2014) 5306–5313, https://doi.org/10.1021/la404765z.

[44] Q. Zhang, X. Wu, Q. Zhang, F. Yang, H. Dong, J. Sui, L. Dong, One-step hydrothermal synthesis of MnO_2/graphene composite for electrochemical energy storage, J. Electroanal. Chem. 837 (2019) 108–115, https://doi.org/10.1016/j.jelechem.2019.02.031.

[45] C. Guan, J. Liu, Y. Wang, L. Mao, Z. Fan, Z. Shen, H. Zhang, J. Wang, Iron oxide-decorated carbon for supercapacitor anodes with ultrahigh energy density and outstanding cycling stability, ACS Nano 9 (2015) 5198–5207, https://doi.org/10.1021/acsnano.5b00582.

[46] X. Xia, Q. Hao, W. Lei, W. Wang, D. Sun, X. Wang, Nanostructured ternary composites of graphene/Fe_2O_3/polyaniline for high-performance supercapacitors, J. Mater. Chem. 22 (33) (2012) 16844–16850, https://doi.org/10.1039/C2JM33064D.

[47] X. Xia, Q. Hao, W. Lei, W. Wang, H. Wang, X. Wang, Reduced-graphene oxide/molybdenum oxide/polyaniline ternary composite for high energy density supercapacitors: synthesis and properties, J. Mater. Chem. 22 (17) (2012) 8314–8320, https://doi.org/10.1039/C2JM16216D.

[48] A. Di Fabio, A. Giorgi, M. Mastragostino, F. Soavi, Carbon-poly (3-methylthiophene) hybrid supercapacitors, J. Electrochem. Soc. 148 (8) (2001) A845–A850, https://doi.org/10.1149/1.1380254.

[49] X. Zhao, C. Johnston, P.S. Grant, A novel hybrid supercapacitor with a carbon nanotube cathode and an iron oxide/carbon nanotube composite anode, J. Mater. Chem. 19 (46) (2009) 8755–8760, https://doi.org/10.1039/b909779a.

[50] K. Zhang, L.L. Zhang, X.S. Zhao, J. Wu, Graphene/polyaniline nanofiber composites as supercapacitor electrodes, Chem. Mater. 22 (4) (2010) 1392–1401, https://doi.org/10.1021/cm902876u.

[51] J. Yan, T. Wei, Z. Fan, W. Qian, M. Zhang, X. Shen, F. Wei, Preparation of graphene nanosheet/carbon nanotube/polyaniline composite as electrode material for supercapacitors, J. Power Sources 195 (9) (2010) 3041–3045. doi:1016/j.jpowsour.2009.11.028.

[52] O. Aaboubi, J. Chopart, J. Douglade, A. Olivier, C. Gabrielli, B. Tribollet, Magnetic field effects on mass transport, J. Electrochem. Soc. 137 (6) (1990) 1796.

[53] R. Aogaki, K. Fueki, T. Mukaibo, Application of magnetohydrodynamic effect to the analysis of electrochemical reactions 2. Diffusion process in MHD forced

flow of electrolyte solutions, T. Denki Kagaku 43 (9) (1975) 509–514, https://doi.org/10.5796/kogyobutsurikagaku.43.509.

[54] O. Devos, O. Aaboubi, J.-P. Chopart, A. Olivier, C. Gabrielli, B. Tribollet, Is there a magnetic field effect on electrochemical kinetics?, J. Phys. Chem. A 104 (7) (2000) 1544–1548, https://doi.org/10.1021/jp993696v.

[55] P. Taberna, P. Simon, J.-F. Fauvarque, Electrochemical characteristics and impedance spectroscopy studies of carbon-carbon supercapacitors, J. Electrochem. Soc. 150 (3) (2003) A292, https://doi.org/10.1149/1.1543948.

[56] K. Gelderman, L. Lee, S. Donne, Flat-band potential of a semiconductor: using the Mott-Schottky equation, J. Chem. Educ. 84 (4) (2007) 685, https://doi.org/10.1021/ed084p685.

[57] M. Itagaki, S. Suzuki, I. Shitanda, K. Watanabe, Electrochemical impedance and complex capacitance to interpret electrochemical capacitor, Electrochemistry 75 (8) (2007) 649–655, https://doi.org/10.5796/electrochemistry.75.649.